TURUN
YLIOPISTO
UNIVERSITY
OF TURKU

VERSATILE ULTRATHIN FILMS OF CONDUCTING POLYMERS BY VAPOR PHASE POLYMERIZATION AT ATMOSPHERIC PRESSURE

Synthesis, Process Optimization, and Characterization

Rahul Yewale

TURUN YLIOPISTON JULKAISUJA – ANNALES UNIVERSITATIS TURKUENSIS
SARJA – SER. AI OSA – TOM. 680 | ASTRONOMICA – CHEMICA – PHYSICA – MATHEMATICA | TURKU 2022

TURUN
YLIOPISTO
UNIVERSITY
OF TURKU

VERSATILE ULTRATHIN FILMS OF CONDUCTING POLYMERS BY VAPOR PHASE POLYMERIZATION AT ATMOSPHERIC PRESSURE

Synthesis, Process Optimization, and Characterization

Rahul Yewale

TURUN YLIOPISTON JULKAISUJA – ANNALES UNIVERSITATIS TURKUENSIS
SARJA – SER. AI OSA – TOM. 680 | ASTRONOMICA – CHEMICA – PHYSICA – MATHEMATICA | TURKU 2022

University of Turku

Faculty of Science
Department of Chemistry
Chemistry
Doctoral programme in Exact Sciences (EXACTUS)

Supervised by

Professor Carita Kvarnström
Department of Chemistry
University of Turku
Turku, Finland

Adjunct Professor Pia Damlin
Department of Chemistry
University of Turku
Turku, Finland

Reviewed by

Professor Krzysztof Winkler
Faculty of Chemistry
Department of Materials Chemistry
University of Bialystok
Bialystok, Poland

Assoc. Professor Trisha Andrew
Department of Chemistry
University of Massachusetts Amherst
Massachusetts, United States

Opponent

Assoc. Professor Anna Maria Coclite
Institute of Solid State Physics
Graz University of Technology
Graz, Austria

ISBN 978-951-29-9091-7 (PRINT)
ISBN 978-951-29-9092-4 (PDF)
ISSN 0082-7002 (Print)
ISSN 2343-3175 (Online)
Painosalama, Turku, Finland 2022

To my mother, brother, and sister

UNIVERSITY OF TURKU
Faculty of Science
Department of Chemistry
Materials Chemistry
Rahul Yewale: Versatile Ultrathin Films of Conducting Polymers by Vapor Phase Polymerization at Atmospheric Pressure: Synthesis, Process Optimization, and Characterization
Doctoral Dissertation, 138 pp.
Doctoral Programme in Exact Sciences (EXACTUS)
November 2022

ABSTRACT

The limitations such as toxicity, brittleness, scarcity, and high cost of currently available materials for energy storage and transparent electrode applications in bendable electronics create a need for green, sustainable, and cost-effective alternatives. Organic conducting polymers (CPs) can transport charge across conjugated sp^2 carbon network. Their low-tuneable band gap, flexibility, and transparency could make them viable alternatives. However, the challenges such as processability, stability, biocompatibility, and production cost remain milestones to achieve. Therefore, this thesis work is an effort toward a green and sustainable future.

Poly(3, 4-ethylenedioxythiophene) (PEDOT), known for its conductivity, robustness, and biocompatibility and polyazulene (PAz), known for its high capacitance are selected for studies due to their unique abilities. Fabrication of highly electrically conducting ultra-thin films of PEDOT is done by developing and optimizing a cost-efficient vapor phase polymerization method at atmospheric pressure (AP-VPP) and combining a layer-by-layer (L-b-L) synthesis approach. As a result, AP-VPP PEDOT films showed comparative sheet resistance, transmittance, and conductivity with commercially available ITO-coated materials. In contrast, the flexible, green organic nature and high capacitance of PEDOT thin films overcome the competition with ITO-coated materials. Similarly, well-organized high-capacitance PAz films are L-b-L synthesized using an optimized AP-VPP process.

The influence of factors such as substrate surface cleaning, oxidant solution, oxidant spin coating rate and time, cell and substrate temperature, polymerization time, drying and annealing temperature and time, air vs nitrogen atmosphere, and washing-solvents on film properties were studied during the optimization process for both the CPs. Properties like optical bandgap, sheet resistance, surface roughness, conductivity, capacitance, and % transmittance provided a route for process optimization. Furthermore, FTIR, Raman, and UV–Vis spectroscopy were utilized to analyse the extended conjugation along with the type and trend in the charge carriers generated upon doping the resulting films. Microscope imaging, AFM, and SEM were utilized to analyse surface morphologies and microstructures. The capacitance properties, transport of counterions across multiple layers, and charge transport resistance were investigated using cyclic voltammetry and electrochemical impedance spectroscopy. In addition, the characterization techniques complement each other in data interpretation. PEDOT and PAz films produced in the present work and their properties are compared with available reports in the literature.

TURUN YLIOPISTO
Matemaattis-luonnontieteellinen tiedakunta
Kemian Laitos
Kemia
Rahul Yewale: Versatile Ultrathin Films of Conducting Polymers by Vapor Phase Polymerization at Atmospheric Pressure: Synthesis, Process Optimization, and Characterization
Väitöskirja, 138 s.
Eksaktien tieteiden tohtoriohjelma (EXACTUS)
Marraskuu 2022

TIIVISTELMÄ

Energian varastointisovelluksissa ja taivutettavassa läpinäkyvässä elektroniikassa tällä hetkellä saatavilla olevien materiaalien rajoitukset, kuten myrkyllisyys, hauraus, niukkuus ja korkeat kustannukset luovat tarpeen vihreille, kestäville ja kustannustehokkaille vaihtoehdoille. Orgaaniset johtavat polymeerit voivat toimia varauksenkuljettajina konjugoidun sp^2-hiiliverkkonsa ansiosta. Niillä on myös alhainen ja muokattavissa oleva energiavyö, ja ne ovat joustavia sekä läpinäkyviä, minkä vuoksi ne voisivat olla käyttökelpoinen vaihtoehto. Haasteet, kuten prosessoitavuus, pysyvyys, yhteensopivuus ja tuotantokustannukset, ovat kuitenkin edelleen virstanpylväitä, jotka on saavutettava. Tämä väitöskirjatyö on pyrkimys kohti vihreää ja kestävää tulevaisuutta.

Johdepolymeerit poly(3,4-etyleenidioksitiofeeni) (PEDOT), joka tunnetaan johtavuudestaan, kestävyydestään ja biologisesta yhteensopivuudestaan, sekä polyatsuleeni (PAz), joka tunnetaan korkeasta kapasitanssistaan, valittiin tähän tutkimustyöhön ainutlaatuisista kyvyistään johtuen. Työssä kehitettiin ja optimoitiin ilmakehän paineessa toimiva höyryfaasipolymerointimenetelmä (AP-VPP), jolla saadaan kustannustehokkaasti valmistettua erittäin sähköä johtavia ja ohuita PEDOT-kalvoja käyttäen kerros kerrokselta (L-b-L) synteesimenetelmää. Tällä menetelmällä valmistettujen AP-VPP PEDOT-kalvojen resistanssi, transmittanssi ja johtavuus ovat vertailukelpoisia kaupallisesti saatavilla olevien ITO-pinnoitettujen materiaalien kanssa. Toisaalta PEDOT-ohutkalvot ovat orgaanisia, joustavia ja niillä on korkea kapasitanssi, minkä ansiosta ne voittavat epäorgaanisen ja hauraan ITO materiaalin. Samaa menetelmää käytettiin myös hyvin järjestäytyneiden korkean kapasitanssin PAz-kalvojen valmistuksessa.

Substraatin pinnan puhdistuksen, käytetyn hapetinliuoksen, hapettimen pyöröpinnoitusnopeuden ja -ajan, kennon ja substraatin lämpötilan, polymerointiajan, kuivaus- ja hehkutuslämpötilan ja -ajan, kennon ilmakehän ja pesuliuottimien vaikutusta kalvon ominaisuuksiin tutkittiin. Prosessissa pyrittiin optimoimaan materiaalin optiset ominaisuudet, resistanssi, pinnan karheus, johtavuus, kapasitanssi ja transmittanssi. Lisäksi FTIR-, Raman- ja UV-Vis-spektroskopiaa käytettiin analysoimaan materiaalin konjugaatiota ja kalvojen seostuksessa syntyvien varauksenkuljettajien ominaisuuksia. Mikroskooppikuvausta, elektronimikroskooppia (SEM) ja atomivoimamikroskooppia (AFM) käytettiin pinnan morfologioiden ja mikrorakenteiden analysointiin. Kalvojen kapasitanssia, vastaionien kulkua eri kerrosten välillä ja resistanssia tutkittiin sähkökemiallisilla menetelmillä, kuten syklisellä voltammetrialla ja impedanssispektroskopialla. Työssä käytetyt karakterisointitekniikat täydentävät toisiaan. Työssä valmistettujen PEDOT- ja PAz-kalvojen ominaisuuksia verrattiin kirjallisuudessa saatavilla oleviin raportteihin.

Contents

Abbreviations

AC	Alternating current
AFM	Atomic force microscopy
AMOLED	Active matrix OLED
APS	(3-amino propyl) trimethoxysilane
APTES	Aminopropyl triethoxysilane
AP-VPP	Vapor phase polymerization at atmospheric pressure
ATR	Attenuated total reflectance
AW	After washing
Az	Azulene
BW	Before washing
BSE	Backscattered electron
CB	Conduction band
CE	Counter electrode
CNT	Carbon nanotube
CP	Conducting polymer
CRT	Cathode-ray tube
CT	Cell temperature
CTR	Charge transfer resistance
$CuBr_2$	Copper (II) bromide
$CuCl_2$	Copper (II) chloride
CV	Cyclic voltammogram/Cyclic voltammetry
CVD	Chemical vapor deposition
DLaTGS	Deuterated lanthanum α alanine doped triglycine sulphate
EDA	Ethylene diamine
EDOT	3,4-Ethylenedioxythiophene
EIS	Electrochemical impedance spectroscopy
Fc	Ferrocene
$FeCl_3$	Iron (III) chloride
FeTOS	Iron (III) p-toluenesulfonate
FTIR	Fourier transform infrared spectroscopy
FTO	Fluorine doped tin oxide
IRAV	IR active vibrations

ITO	Indium tin oxide
H_2O_2	Hydrogen peroxide
HOMO	Highest occupied MO
iCVD	Initiated CVD
L-b-L	Layer-by-layer
LCD	Liquid crystal display
LD	Lethal dose
LED	Organic light-emitting diode
LUMO	Lowest unoccupied MO
MCT	Mercury-cadmium-telluride
MeCN	Acetonitrile
MO	Molecular orbital
n-BuOH	n-Butanol
NIR	Near-infrared
NH_40H	Ammonium hydroxide
oCVD	Oxidative CVD
OLED	Organic light emitting diodes
PAz	Polyazulene
PEDOT	Poly(3,4-ethylene dioxythiophene)
PEG	Poly(ethylene glycol)
PET	Poly(ethylene terephthalate)
piCVD	Photo-initiated CVD
PPG	Poly(propylene glycol)
PSS	Polystyrene sulphonate
PT	Polymerization time
Pt	Platinum
Py	Pyridine
RE	Reference electrode
RT	Room temperature
SE	Secondary electron
SEC	Spectro-electrochemistry
SEM	Scanning electron microscopy
ST	Substrate temperature
$TBABF_4$	Tetrabutylammonium tetrafluoroborate
TBATOS	Tetrabutylammonium paratoluenesulfonate
TDAE	Tetrakis (dimethylamino)ethylene
TFT-LCD	Thin film transistor-LCD
TOS^-	Para toluene sulphonate anion or tosylate anion
UV-Vis	Ultraviolet-Visible spectroscopy
VB	Valance band
VPP	Vapor phase polymerization

VVPP	Vacuum VPP
WE	Working electrode
xL	‘x’ number of layers
ZnSe	Zinc selenide

Symbols

A	Area of the electrode
Ag	Silver
Ar	Argon
C_A	Areal capacitance
C_V	Volumetric Capacitance
E_g	Bandgap
eV	Electronvolt
Q	Charge
P	Specific resistance
s	Film thickness
V	Volume of the electrode (in cm^3)
ΔV	Potential window
v	Scan rate
RMS	Root mean square
R_a	Roughness average
F	Farad
g	Gram
h	Hour
kΩ	Kiloohm
mF	Millifarad
MΩ	Megaohm
mV/s	Millivolt per second
N_2	Nitrogen
nm	Nanometer
S/cm	Siemens per centimeter
µm	Micrometer
π	Bonding band
π*	Antibonding band
ρ_{sheet}	Sheet resistance
σ	Conductivity
Ω/sq	Ohms per square

List of original publications

This dissertation is based on the following original publications, which are referred to in the text by their Roman numerals:

I **Rahul Yewale**, Pia Damlin, Mikko Salomäki, Carita Kvarnström, "Layer-by-layer approach to engineer and control conductivity of atmospheric pressure vapor phase polymerized PEDOT thin films," Materials Today Communications 25 (2020) 101398

II **Rahul Yewale**, Pia Damlin, Milla Suominen, Carita Kvarnström, "Fabrication of electroactive multi-layered polyazulene thin films by atmospheric pressure-vapor phase polymerization." Materials Chemistry and Physics 275 (2022) 125292

III **Rahul Yewale**, Pia Damlin, Carita Kvarnström, "Effect of oxidant on properties of electroactive ultrathin polyazulene films synthesized by vapor phase polymerization at atmospheric pressure" (accepted for publication in Langmuir)

Contribution of the author:

PAPER I: The author executed the conceptualization, design of the work, data collection, formal analysis, and interpretation, drafting the article, critical revision of the article, final approval of the version to be published together with supervisors.

PAPER II: The author executed the conceptualization, design of the work, data collection, formal analysis, and interpretation, drafting the article, Critical revision of the article, final approval of the version to be published together with supervisors.

PAPER III: The author executed the conceptualization, design of the work, data collection, formal analysis, and interpretation, drafting the article, Critical revision of the article, final approval of the version to be published together with supervisors.

List of other related publications

Milla Suominen, Suvi Lehtimäki, **Rahul Yewale**, Pia Damlin, Sampo Tuukkanen, Carita Kvarnström, *"Electropolymerized polyazulene as active material in flexible supercapacitors"*, Journal of Power Sources 356 (2017) 181-190

Rahul Yewale, Pia Damlin, Carita Kvarnström, "Pseudo behaviour of anodic peak currents of Polyazulene thin films as function of oxidant induced microstructural and chemical film-modifications" (To be submitted)

WO2019211509 - METHOD FOR PRODUCING A PEDOT FILM (PCT/FI2018/050330)

WO2019211510 - METHOD FOR PRODUCING A POLYMER FILM (PCT/FI2019/000006)

WO2020221958 - METHOD FOR FABRICATING A FILM (PCT/FI2020/050261)

FI20225704 - A METHOD FOR MANUFACTURING A PATTERNED POLYMER FILM STRUCTURE (in progress)

1 Introduction

Today, electronic displays and touch screens are entirely unified in daily life and in several applications across the industrial sector. They are established and employed in all societal sectors, e.g., education, health care, transportation, automotive, sports and entertainment events, smartphones, and computers. The foremost applications driving the market are cell phones/smartphones, automotive displays, computing devices, e-readers, smart televisions, government agencies, retail and corporate establishments, transportation industry, health care institutions, and upcoming flexible devices.

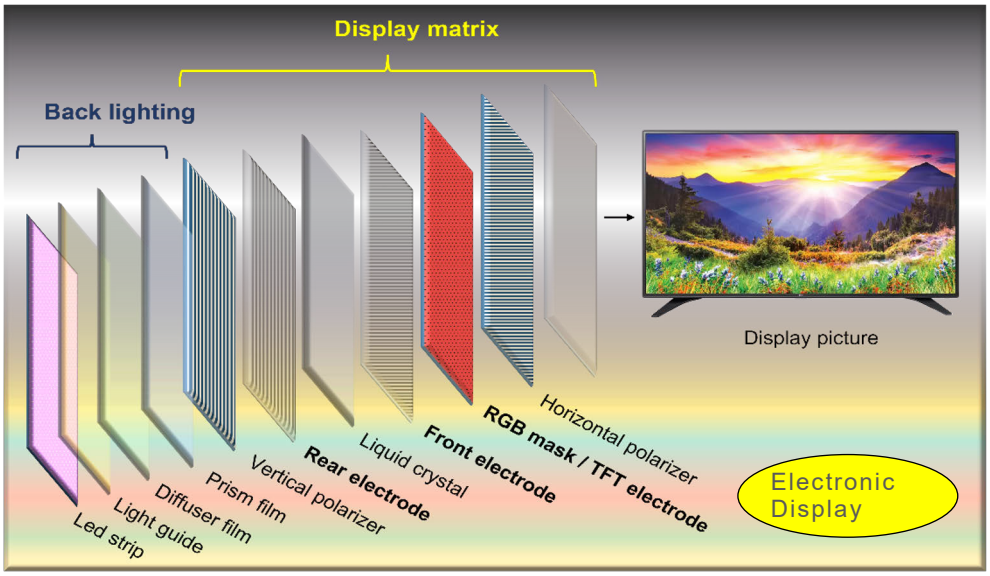

Figure 1. A general schematic of electronic display.

Modern electronic displays have replaced conventional displays such as galvanometers, counters, and paper displays. **Figure 1** shows the schematic of an electronic display. Over the last few decades, the field has evolved from monochrome cathode-ray tube (CRT) and monochrome plasma display to thin-film transistor liquid crystal

display (TFT-LCD), full-colour plasma display and to organic light-emitting diode (OLED) / active matrix-OLED (AMOLED) displays [1–6]. The AMOLED, OLED, and micro-LED are examples of cutting-edge high-resolution display technology developments [1,4,7]. The advanced displays are energy-efficient, low on maintenance, comparatively affordable, and more durable than traditional displays. In addition, technical innovation brought in a profound turn from conventional sluggish and inaccurate resistive mono-touch screens to very sensitive multi-touch capacitive smart touch screen displays [8–13]. Furthermore, capacitive touchscreens benefit from the limitations of acoustic wave touchscreens, such as error, mono touch, tap strength, versatility, and touch-hold [8,10]. Touch screens have simplified and accelerated the use of the internet of things (IoT) through a direct interaction of a user-friendly interface. **Figure 2** shows the schematic of a touchscreen which can be used individually or integrated with a display.

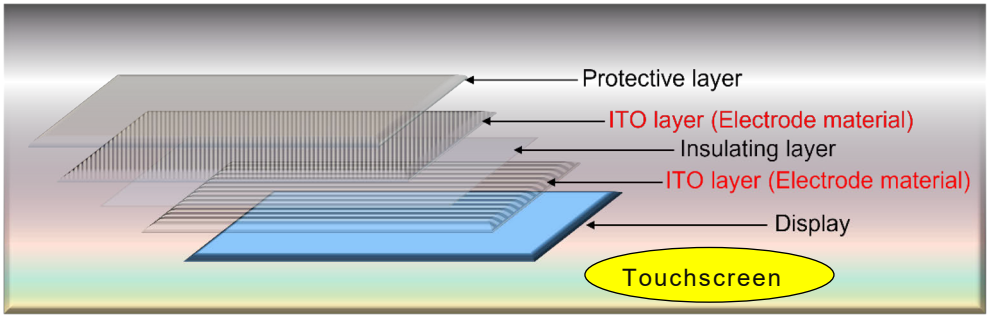

Figure 2. A schematic of touchscreen.

Due to the challenges in energy consumption and its green source alongside technological development and improved lifestyle, the need for energy storage and transport devices such as advanced batteries and supercapacitors is simultaneously growing [14–18].

Figure 3 shows the schematic of smart glass and supercapacitor. The growth of the smart glass market and optimal energy saving through innovative glass applications is mainly driven by applications in automobiles, ships, aeroplanes, and energy-efficient infrastructures [19–24]. As a result, market sizes of electronic displays [25], touchscreens [26], smart windows [27], and energy storage devices [28–30] are billions of euros and growing with tremendous speed. This rapid evolutions in markets demand heavy raw material inflow, green resources, low-cost production, and minimal damage to the environment.

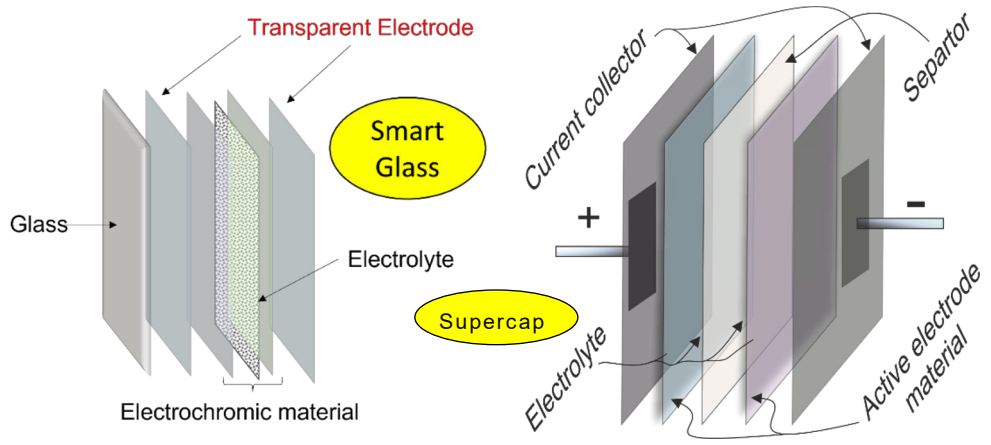

Figure 3. A schematic of smart glass and supercapacitor-

Indium tin oxide (ITO) is well-known electrode material used in touchscreens, electronic displays, and emerging smart glasses with well-known processing technology and efficiency [31,32]. Even though there is massive use of ITO materials in various electronics, little is known about the toxicity of ITO. Recent toxicological studies show bioaccumulation and lung diseases such as pulmonary fibrosis and pneumonia caused by ITO exposure [33–37]. The use of silver nanowires and carbon nanotubes (CNTs) as electrode materials for the same applications has been growing [38–41]. Various scientific articles have reported the toxicity of CNTs, such as bioaccumulation, mitochondria damage in rat-brain, genotoxicity, cytotoxicity, and pulmonary toxicity [41–43]. Furthermore, toxicity reports of silver nanoparticles include damage to plants and aquatic life, bacteria, rat brain damage, swelling, and oxidative stress in cells [41,44,45].

Along with the common toxicity attribute, the brittleness of these materials limits their applications in flexible devices. Flexible devices are the next level of evolution in a technology-driven world. Moreover, rare earth elements are limited to specific geographical areas. Material efficiency, scarcity of raw materials, high-cost synthesis, stabilizers, and storage are increasing the time and cost of manufacturing. Clearly, sustainability and green resources remain a challenge, and there is a requisite for cost-effective and sustainable alternatives. The need for novel and electrically conducting, transparent, and flexible thin films as electrode material produced in a very cost-efficient way and suitable for electronic displays, touch screens, smart windows, and supercapacitors remain the aim of this thesis. And a thought at this point was whether conducting polymers can qualify as an alternative material to available transparent electrode materials.

This thesis focuses on the need for new electrically conductive, transparent, and flexible thin films that can be applied as electrode material in displays, touch screens,

smart windows and supercapacitors. Furthermore, these electrode materials should also be able to be manufactured very cost-effectively. This work considered whether conductive polymers could be accepted as an alternative material to the available transparent electrode materials.

1.1 Conducting polymers

Electrically conducting polymers, widely mentioned as conducting polymers (CPs), are the polymers containing conjugated sp^2 carbons with low-tuneable bandgap and overlapping molecular orbitals with delocalized electrons that allow transport of charge upon tuning the properties. They are also described as synthetic metals or organic semiconductors. In the search for a covalent organic polymer possessing metallic conductivity, Hideki Shirakawa, Alan G. MacDiarmid, and Alan J. Heeger et al. focused on polyacetylene [46]. They obtained a systematic increase in conductivity of seven to eleven orders of magnitude in polyacetylene by exposure to halogen vapour and by using different dopants [46,47]. Heeger, MacDiarmid and Shirakawa were awarded the Noble Prize in Chemistry in 2000 by the Royal Swedish Academy of Sciences for their work and developments in electrically conductive polymers during the 1970s and beyond [48]. The added holes or extra electrons, while doping (during the process of removal or addition of electrons through oxidation or reduction), can move along the conjugated polymer backbone and are the key to obtaining highly conducting polymers. Chemical or electrochemical p-doping of CPs can be achieved by oxidation which leads to positively charged conjugated structures with concurrent charge compensation by anions out of coulombic interactions for electroneutrality. Similarly, chemical or electrochemical n-doping can be obtained by reduction, resulting in a negatively charged conjugated polymer backbone with simultaneous charge compensation by cations. The source of doping ions can vary depending on the reaction media, e.g., electrolyte anions during electrochemical p-doping and cations during n-doping can compensate the positive/negative charge developed in the polymer backbone by intercalation under the applied electrochemical potential. Additional information about the optical and electrochemical bandgaps of CPs and formation of charge carriers due to doping is briefly discussed in the spectroscopic characterization section (Chapter 5).

The ability of thin films of CPs to transport charge is reliant on many factors such as effective conjugation length, cross-linking, defects, uniformness, morphology, inter-chain interactions, charge compensation by dopant ions, properties of dopant ions and charge carriers generated, reaction medium induced changes, etc. The change in properties of CPs with the length of extended conjugation and after fine-tuning them to their partial to complete -neutral, reduced, and oxidized states open various fields of applications. The important expanding areas of practical

applications of CPs include antistatic coatings, energy storage, light emitting diodes (LEDs), molecular electronics, optoelectronics, sensors, and organic solar cells. CPs are known for their transparency, flexibility, electrical conductivity, capacitive behaviour, redox nature, low bandgap, and biocompatibility. In the present thesis, we have studied poly(3,4-ethylene dioxythiophene) (PEDOT) and polyazulene (PAz).

1.2 PEDOT

3,4-ethylene dioxythiophene (EDOT) is the repeating monomer unit of PEDOT with electron-donating lone pair of a sulphur atom and ethylenedioxy-ether group at β, β' position; give α, α' −connectivity upon polymerization (**Figure 4**a and b). The ethylenedioxy bridge attached at the 3- and 4-positions of the thiophene not only prevents the undesired α, β- and β, β-couplings within the polymer backbone, giving the polymers a high degree of regioregularity but also decreases the oxidation potential of the monomer. Biocompatibility and robustness give PEDOT additional benefits in the diversification of applications. The electrical conductivity and optical activity of PEDOT exceed other competitor-CPs such as polyaniline (1900 S/cm) and polypyrrole (1600 S/cm) [49–51]. PEDOT holds one of the highest reported electrical conductivities among CPs (up to 4500 S/cm) [50,52–56]. It possess an enormous future potential to replace ITO-coated electrodes, silver nanowires, and carbon nanotubes in bendable electronics, optoelectronics, energy storage, and electronics [52,57–63]. The reports of PEDOT applications in electrochemical transducers [60,64], electrochromic and electroluminescent devices [50,58,65], OLEDs [53,62], optoelectronics [61], antistatic coatings [66], solar cells [67], supercapacitors [57,68,69], and thermoelectric composites [70] prove the former statement. A high stability of CPs is needed for their practical applications, and PEDOT shows high stability in the oxidized form [71,72].

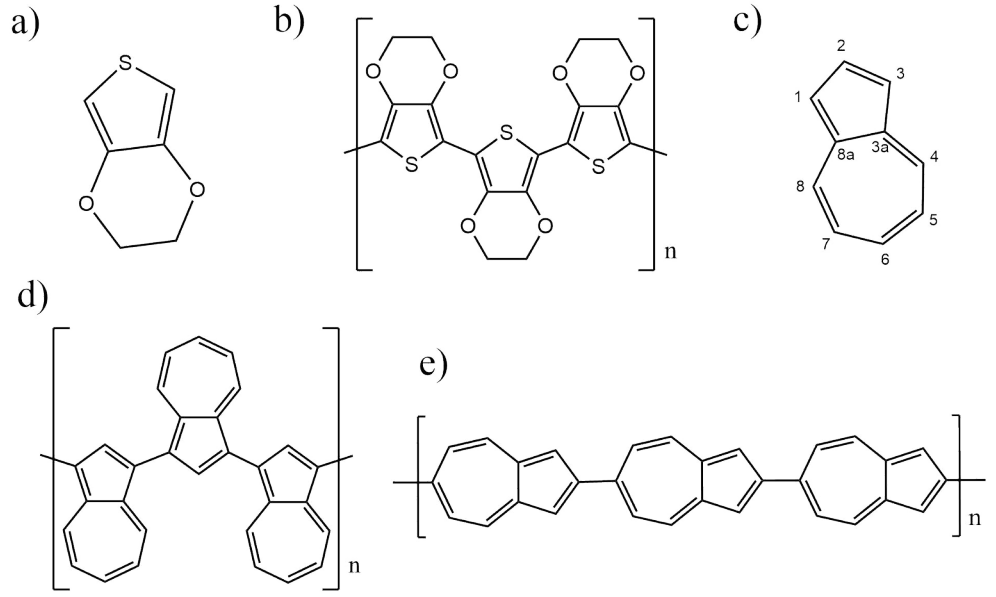

Figure 4 Structure of **a)** EDOT, **b)** PEDOT (In neutral state), **c)** azulene, and **d)** 1,3- and **e)** 2,6-connectivity polyazulene (in neutral state).

1.3 PAz

Azulene (Az) is a fused ring and non-benzenoid aromatic compound consisting of five-membered electron-rich and seven-membered electron-deficient rings (**Figure 4**c). Az is an isomer of naphthalene, a polarised entity with a dipole moment of approximately 1.08 D. Upon polymerization, the 1, 3- connectivity or 2, 6- connectivity gives 1, 3- or 2, 6- PAz, respectively (**Figure 4**d and e) [73–75]. PAz, with the extended conjugation and p/n-dopable properties, show fast charge-discharge behaviour and is an understudied CP. Previous studies show applications of PAz in energy storage and ion-to-electron transducer in calcium selective solid contact electrodes due to its high capacitance, redox behaviour, and hydrophobicity in an aromatic form [76–81]. In addition, applications in antistatic coatings, electronics, solar cells, and electrochemical transducers can utilize the electronic and fast redox properties of PAz. The high capacitance of PAz (400 F/g, 27-55 mF/cm^2) makes it an interesting candidate for applications as electroactive material for supercapacitor and hybrid batteries [77,80,82].

1.4 Toxicology of EDOT and Az

Toxicity studies of EDOT and Az are not very intensively reported. Therefore, thorough research in the near future on these materials' hazards and toxicity is necessary.

However, the following information has been gathered according to the published reports, which proves that these materials are not harmful.

The lethal dose 50 (LD50) oral of Az is >4g/kg and EDOT is 615 mg/kg for rat [83,84]. Additionally, LD50 dermal of EDOT is 849 mg/kg for rats [83]. These values are less than those reported for the ITO, CNTs, and Ag nanoparticles [85–89]. Azulene and its derivatives, including guaiazulene or chamazulene, naturally occur in many plants and mushrooms, which have been used for centuries in medicinal purposes[90,91]. Azulene is non-steroidal anti-inflammatory agent [91]. Azulene and its derivatives and conjugates with biologically active compounds are used in medicine in different applications such as anti-inflammatory with peptic ulcers, antineoplastic with leukaemia, antidiabetic, antiretroviral, antimicrobial, antifungal, antiallergic, antibacterial, and anti-inflammatory medicines [90,91].

Extensive applications of PEDOT and PEDOT-based nano materials, such as scaffold implants in bioelectronics as an alternative to metallic microelectrodes and an interface for electronic devices with biological matter in vitro and in vivo, have been reported [92–94]. PEDOT-based bioelectronics has progressed from neural probes in 2003 to the electrodes on the human brain in the last two decades. Even US FDA approved a PEDOT-based coating for medical applications in 2016. Superior electrochemical properties of PEDOT, such as stimulation of electrically active cells or diminishing electrochemical impedance and improving charge injection, have attracted applications as a functional coating for bioelectronics [92–94]. These developments of PEDOT prove its biocompatibility.

2 Synthesis of PEDOT and PAz

2.1 Available methods and techniques

Depending on the application, CPs are synthesized using chemical, electrochemical, dip/spin -coating, and vapour phase polymerization techniques. Furthermore, chemical synthesis includes chemical reagent-initiated polymerization, on-surface synthesis, different types of chemical vapor deposition, and photochemical polymerization.

Electrochemical synthesis: Electrochemical synthesis by anodic oxidation is a commonly used electrochemical synthesis technique in research laboratories for PEDOT and PAz. Factors such as monomer concentration, current, electrochemical potential, scan rate, solvent, supporting electrolyte, temperature, and time govern the properties in the resulting CP film formed on the conducting electrode surface. Although electrochemical polymerization is a well-known and widely used method for PEDOT and PAz synthesis among the available methods, surface roughness and scalability remain the challenge. The electrochemical synthesis of PAz produces grainy microstructures and a film-thickness in the range of micrometres [80,95]. An increasing film thickness affects the transport of ions across the film, and the thicker films often turn out to be brittle.

Chemical synthesis: In chemical synthesis, solvents used in the reaction medium, chemical reagent, temperature, and polymerization time are crucial factors to control properties in the resulting polymer material. Most common oxidants such as $FeCl_3$, FeTOS, Cl_2, and I_2 are used in oxidative chemical synthesis to induce polymerization and provide partial charge-compensating counter ions. Oxidative chemical synthesis of CPs gives the polymer material in powder or granular forms or in a solution state which can be further processed for various applications [73,76,96]. However, the insoluble nature of PAz makes casting or processing impractical.

Chemical vapor deposition (CVD): CVD is a widely accepted, well-known technology for inorganic thin film deposition and is prevalent in the semiconductor industry. By controlling the vapor phase precursors and feed gases, impurities and defects can be controlled in the deposited films. Polymers can be vapor phase deposited on the substrate surface by CVD. Polymer CVD is further divided into two types: initiated and oxidative chemical deposition (iCVD and oCVD) [97].

In iCVD, flow controllers control a mass of monomer and initiator (typically peroxide initiator such as tert-butyl peroxide). In contrast, in photo-initiated CVD (piCVD), substrate irradiation by UV light is used. Initiator-generated radicals further react with precursors to produce radicals, and the subsequent reaction allows polymerization. The lower temperature of a substrate helps deposit the polymer on its surface. In addition, the lower vapor pressure of deposited polymer than the precursors prevent its depletion (by evaporation) back into the reactor. Usually, 0.1 to 1 μm films are produced at the rate of 10 to 100 nm/min using iCVD [97].

In oCVD, controlled monomer flow and thermally evaporated solid-state oxidant (e.g., $FeCl_3$, $CuCl_2$) vapor, spontaneously react to generate radical cations and continue to polymerize at the surface of the substrate with counter ions balanced charge in polymer backbone (doping) [97,98]. PEDOT can be deposited using both iCVD and oCVD. Conductivity as high as 1000 S/cm can be obtained in PEDOT films deposited by oCVD [97].

The chemical vapor deposition (CVD) technique works at high temperatures, making the polymerization rate challenging to control. Besides, a need for a highly sophisticated reactor equipped with temperature and pressure control accessories and limited substrate choice raises the cost of manufacturing [97,99–102].

Dip/spin/shear-coating: One alternative way to produce thin films of CPs is the dip/spin/shear-coating technique. High transmittance and homogeneity can be obtained in the dip/spin-coated PEDOT:PSS (polystyrene sulfonate) films. The characteristic status of low electrical conductivity of PEDOT:PSS films has been changed in recent studies, and conductivities higher than 3000 S/cm have been reported [103–105]. Despite this progress, reproducibility and scalability for fine applications on large surfaces (such as in displays, smart windows, transparent touch panels) remain challenging.

Vapor phase polymerization (VPP): Generally, in VPP, after washing and cleaning the substrate to remove dirt and impurities from the surface, the substrates are often additionally plasma treated to remove any foreign contaminants left behind on the surface. Sometimes the substrate is further coated or treated to increase the adhesion strength of a CP film to a substrate surface. (e.g., ITO/silicon coated glass surfaces, ethylene diamine treated poly(ethylene terephthalate) (PET) films, polymer/surfactant linked surfaces). A substrate containing aromatic rings in its structure gives good adhesion and hardness to CP film as some oxidants may create an active site on the aromatic ring for adhesion. In this case, there is no need for extra linkers or binder molecules.

Table 1. List of some oxidants, organic solvents, and base inhibitors used in the synthesis of CPs by VPP.

Oxidants	Organic solvents	Base inhibitors
Iron tosylate, iron triflate, iron chloride, iron perchlorate, tosylic acid, halogens, molybdophosphoric acid, ammonium persulfate, cerium ammonium nitrate, tartaric acid, polyacrylic acid, naphthalene sulfonic acid, camphor sulfonic acid, cerium sulphate	n-butanol, methanol, isobutanol, 2-ethoxy ethanol, ethanol, cyclohexane, ethyl acetate, toluene, acetonitrile, and butanone	Dimethyl formamide, n-methyl pyrrolidinone, pyridine/imidazole/pyrrole-based compounds, water vapor, glycerol, and glycol derivatives

Table 1 shows a list of the oxidants, solvents (used to prepare oxidant solution), and base inhibitors found in the literature for VPP of CPs. Amine-based compounds and nitrogen atom-containing saturated or unsaturated heterocyclic compounds can be used as base inhibitors with oxidants, which may decrease the oxidant's activity and lower the polymerization rate, subsequently altering the properties of a deposited polymer. Oxidant solution can be spin/dip coated on a substrate. Spinning/dipping rate and time influence the thickness (concentration) of the oxidant film, which impacts on the final properties of a polymerized film. Moreover, the spin-casted oxidant with different additives showed variation in the morphology of oxidant film, and their impact remained throughout the polymerization process until completion [106].

In **Table 2**, a list of various combinations of the oxidant solutions and additives mentioned above, together with the method and substrate material used and their influence on the properties of the obtained PEDOT films, are given. In **Table 2**, the use of FeTOS with pyridine (Py) can be observed to yield high conductivities in the resulting PEDOT films. Various combinations of oxidant solution and additives can be used in order to tune the conductivities in CP films. E.g., high conductivity (1500 S/cm) of PEDOT was also obtained using amphiphilic copolymer instead of pyridine with oxidant to maintain liquid-like properties of oxidant [107]. In this bottom-up process, renewed oxidant surface through capillary transport of oxidant to the surface with the merging of PEDOT grains facilitated continuous polymerization [107]. Additionally, using an optimum concentration of such amphiphilic copolymers or surfactants (PEG-PPG-PEG) reduces the oxidant reactivity by complexation and increases the conductivity by improving the conjugation length and doping [50,108]. Drying the oxidant film in an oven or on a hot plate after spin coating removes the solvent traces and volatile impurities. The oven vacuum chamber is maintained at a specific temperature during polymerization. The polymerization process can take up to an hour, depending on other process parameters. Inert gases such as nitrogen (N_2) or argon (Ar) gas are purged into the chamber in partial vacuum conditions. Annealing on a hot plate after polymerization prevents stress fracturing of the film during

washing. Rinsing with solvent removes unreacted monomer, volatile impurities, and undesired side products. After rinsing, the substrate is dried to evaporate washing-solvent traces. Post-treatment with acids has shown increased conductivity in the resulting polymer film. Solution-processed polymer films are usually post-treated. Sheet resistance, transmittance, and conductivity of CP films can be controlled by regulating the reaction temperature, combinations of oxidants and additives, and improving the morphologies and film thicknesses.

A vacuum vapor phase polymerization (VVPP) technique requires a reactor equipped with a vacuum generator, pressure, and temperature controls with extensive polymerization time [50,108,109]. These challenges are addressed in the present thesis by developing and optimizing the vapor phase polymerization method at atmospheric pressure (AP-VPP) for PEDOT and PAz.

2.2 AP-VPP of PEDOT and PAz

Our homemade and optimized AP-VPP is simple, cost-effective, and fast. An oxidant-coated substrate is exposed to monomer vapor at atmospheric pressure to form a thin layer of the polymer. After the polymerization, a substrate containing a polymer film is annealed to avoid stress fracture, followed by washing and drying. Few nanometers thick, uniform, and transparent CP films are produced with a controlled polymerization rate by regulating temperature and other method parameters.

The proposed mechanism[66,110] of oxidative polymerization for PEDOT shows that the oxidant-catalyzed generation of EDOT radical cations undergoes dimerization with the loss of two protons. Further end-group oxidation of oligomers and loss of protons give higher oligomers and, ultimately, polymers in a continuous process. Simultaneously, doping of the positively charged thiophene ring along the conjugated backbone can take place by oxidant anions (dopant ions) to balance the charge. This oxidative polymerization of EDOT produces PEDOT in its neutral to partially doped state. Forced oxidation can enforce the additional doping state in the polymer.

The AP-VPP method enables the engineering of PEDOT and PAz films at nanometers to micrometers thickness-scale on different substrates such as bendable, conducting-nonconducting, plastic, fabric, glass, metal, paper, and wooden substrates. The scaled-up process successfully produced PEDOT films on PET surfaces as large as 484 cm^2. We utilized AFM and SEM to study the films' structural properties and surface morphologies. Fourier transform infrared (FTIR), Raman, and UV-Visible (UV-Vis) measurements were carried out to investigate the optical and chemical properties of the films. Electroactivity and capacitance properties were determined by using cyclic voltammetry (CV) and electrochemical impedance spectroscopy (EIS). Sheet resistance and transmittance remained the tools for optimizing

method parameters. The effect of multiple layers on the film properties like optical bandgap, sheet resistance, electrical conductivity, surface roughness and transmittance are evaluated by using respective characterization techniques. **Table 2** provides the compilation of controlled environment VPP, partial VVPP, humidity-facilitated VPP, and oCVD techniques, together with the developed AP-VPP used in this thesis work.

The plasticity of organic polymers and the possibility of vapor phase deposition onto limitless substrates is an excellent advantage over ITO-coated materials. PEDOT-coated PET showed an insignificant decrease in conductivity upon 1000 compressive bending phases, whereas ITO-coated PET exhibited 400 times lower conductivity because of cracking [111].

Table 2. Compilation of PEDOT films synthesized using various vapor phase deposition techniques with AP-VPP (abbreviations used in the table are as follows: Py; pyridine, PET; polyethylene terephthalate, EDA; ethylene diamine, APS; (3-amino propyl) trimethoxysilane, TDAE; Tetrakis (dimethylamino) ethylene, APTES; Aminopropyl triethoxysilane, PEG-PPG-PEG; poly(propylene glycol)-poly(ethylene glycol)-poly(propylene glycol)). Note: Cntr. Env.: air/N_2/Ar [54], N_2 [61], N_2 [112], Ar [113], N_2 [114], N_2 [115].

Type	Substrate	Oxidant + Inhibitor	Poly. Time (min)	ρ_{sheet} (Ω/□)	σ (S/cm)	Addi. comments	Ref.
AP-VPP	Microscope glass slide	FeTOS + Py	4 - 24	195 - 21	2178 - 3208	Layer-by-layer synthesis (23 to 152 nm)	Paper (I) [56]
Contr. Env. VPP	PET, Pt coated PET	FeTOS + Py	60	-	1000	Film thickness 250 nm	[54]
VPP	Microscope glass slide	FeTOS + Py	60	-	775	Film thickness 60 nm	[116]
Contr. Env. AP-VPP	EDA treated PET, glass	FeTOS + Py + glycerol	30	400 - 1200	50 - 500	Film thickness 50 to 200 nm	[61]

Type	Substrate	Oxidant + Inhibitor	Poly. Time (min)	ρ_{sheet} (Ω/□)	σ (S/cm)	Addi. comments	Ref.
VVPP	Glass	FeTOS + (PEG-PPG-PEG)	25	-	50 - 1487	H_2O vapor, PEDOT-triblock co-polymer, film thickness 50 to 75 nm	[108]
VVPP	Microscope glass slide	FeTOS + (PEG-PPG-PEG) + C1 to C8 alkanols	25	45	3400	PEDOT-triblock co-polymer, film thickness 65 nm	[50]
Partial vacuum with contr. humidity VPP	Silicon-titanium mixed oxide-coated glass	FeTOS + Py	15 - 75	279 - 5625	162 - 1354	Film thickness 15 to 70 nm	[52]
AP-VPP	PET film	$FeCl_3$	2 - 15	74 - 620	810 - 1500	After 24 h acid treatment (50 Ω/□ and 2200 S/cm)	[53]
VVPP	Microscope glass slide	FeTOS + 2D nano material (graphene + MoS_2)	25	-	1000 - 2160	Graphene + PEDOT + MoS_2 composite film	[117]
Contr. Env. VPP	Glass plate	FeTOS + Py	25	-	4 - 290	EDOT + Pyrrole, Film thickness 104 to 143 nm	[112]
Contr. Env. VPP	Polyacrylonitrile Mats	FeTOS + Py	15 - 90	-	1 – 26	EDOT, Pyrrole, thickness 5 to 12 nm	[113]
(Parameters not given) VPP	APS modified SiO_2 coated Si	FeTOS + Py, PSS, Ethylene glycol	2 - 80	-	500 - 680 S/cm	Film thickness 30 to 180 nm	[118]

Type	Substrate	Oxidant + Inhibitor	Poly. Time (min)	ρ_{sheet} (Ω/□)	σ (S/cm)	Addi. comments	Ref.
Humidity facilitated VVPP	Glass, ITO coated glass	FeTOS + Py + PEG-PPG-PEG	30 + 60	-	145 - 360 S/cm	Film thickness 90 to 185 nm	[109]
Chemical synthesis	Glass	FeTOS + Py	72 h	-	300	TDAE reduced films,	[119]
oCVD	Glass and silicon	$FeCl_3$ and Br_2	20 – 40	-	40 - 380	Film thickness 40 nm	[98]
oCVD	Glass	$FeCl_3$	-	150 – 6 k	300 - 1400	Film thickness 50 nm	[99]
oCVD	ITO coated glass	$FeCl_3$	30	-	-	Film thickness <500 nm	[100]
Contr. Env. VPP	Glass plate	FeTOS + Py	30	-	30 - 500	Film thickness 25 to 191	[114]
Unclear VPP	PET film	FeTOS, $CuCl_2$	30		20 - 260	Film thickness 100 to 130 nm	[120]
Contr. Env. VPP	PET film	FeTOS	10	90 – 182 k	1 - 142	EDOT + APTES, 65 to 250 nm	[115]

3 Materials and methods

A detailed description of materials used in the experiments is given in the respective original publications (Paper I to III).

3.1 Process parameters for AP-VPP

All the parameters are optimized, and detailed information for the PEDOT films is provided in Paper-I, and for PAz films, in Paper-II. In addition, a summary and the schematic of the AP-VPP procedure used in synthesizing thin films of PEDOT and PAz are also provided in **Figure 5**.

a) Substrate cleaning: Microscope glass slides of 2.54 × 2.54 cm (substrates) or desired sizes are cleaned by ultrasonication in acetone, water, and ethanol, respectively, each for 5 min. These cleaned glass substrates are dipped in hot solution (80 °C) of 5[H_2O]:[25 % NH_4OH]:[30 % H_2O_2] (volume ratio) for 5 min.

b) Drying: The cleaned substrates are rinsed and left for drying, covered under a skewed beaker.

c) Oxygen plasma treatment: Dried substrates are oxygen plasma treated for 3 to 5 min.

d) Oxidant coating: The oxidant solution* (which may contain an inhibitor*) was prepared in n-BuOH. The cleaned substrate was spin-coated with 'X'* µl of oxidant solution at 2400 rpm for a specific time (see the manuscripts).

e) Oxidant drying: The oxidant-coated substrate was dried on a hot plate at 90 °C for 90 s.

f) Polymerization: The dried substrate was immediately moved to a preheated VPP cell (**Figure 5**) containing monomers at 'T'* °C. The polymerization time is provided in the respective manuscripts. A temperature-controlled copper block is utilized to regulate the temperature of the substrate.

* Refer to the manuscripts for optimized values of parameters.

g) Annealing: In the following step, an oxidant-coated substrate containing the polymer film was annealed* on a hot plate at 90 °C for 90 s. The polymer film is then let to cool down to room temperature.

h) Washing: the annealed polymer film is dip-washed carefully in washing solvents* to remove oxidant, monomer, and other impurities/by-products.

i) Drying: The substrate containing polymer thin film is dried under a dry nitrogen gas stream to remove the traces of washing solvents.

j) Storage: The substrates containing polymer thin film are always stored in a desiccator.

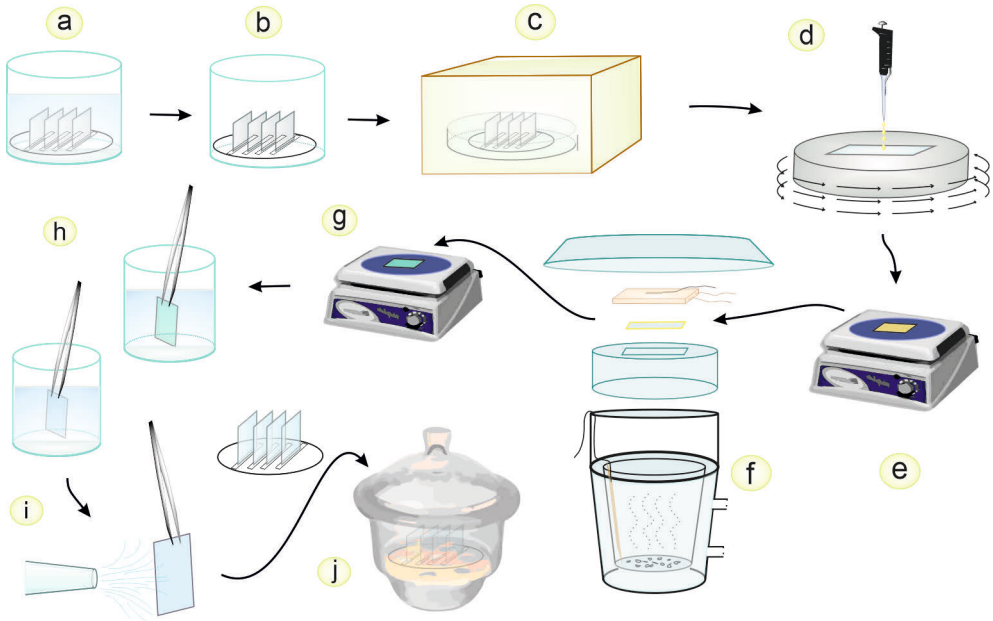

Figure 5. Steps in AP-VPP procedure marked with **a** to **j.** These different steps are explained in the texts above.

The procedure is repeated from the spin coating step to produce multi-layered films. Separate thermostat baths are employed to control the cell and copper block temperature.

We used short labelling for easy comparison between the films. For example, the label '3L PAz (60 mM $CuCl_2$)' refers to the 'three-layered PAz film synthesized by using 60 mM of $CuCl_2$ as an oxidant' via AP-VPP. Hereafter, all the films are explained by using their short labels.

4 Instrumentation

Agilent 8453 spectrometer was utilized to record UV-Vis spectra of AP-VPP PEDOT and PAz films synthesized on a glass substrate.

FTIR spectra were recorded from thin CP films on FTO glass substrates by **Bruker Vertex spectrometer** using a Harrick Seagull variable angle reflection accessory and liquid nitrogen cooled MCT (mercury-cadmium-telluride) detector. Measurements were performed at 50º to 85º (using 5º increments) angle of incidence relative to the surface normal with 4 cm^{-1} spectral resolution and 256 scans. In addition, a Harrick Diamond FTIR-ATR (attenuated total reflectance) accessory with an RT-DLaTGS (room temperature - deuterated lanthanum α alanine doped triglycine sulphate) detector was used for the powder samples. A total of 32 to 256 interferograms were co-added using 4 cm^{-1} as a resolution in the 400 – 7000 cm^{-1} range.

Renishaw Qontor inVia Raman microscope equipped with Leica microscope, a CCD (charge coupled device) detector, 20X objective, 1200 and 1800 l/mm grating and 532 nm and 785 nm as excitation source were used to record Raman spectra at room temperature.

Microscope images were acquired at room temperature using **a Leica microscope** (20X objective).

AFM measurements were carried out using **Veeco diCaliber scanning probe microscope** operated in a tapping mode at room temperature. All AFM images were recorded using Bruker TESP-MT probe (resonant freq. 320 kHz, spring const. 42 N/m, length 125 µm, width 30 µm, Cantilever spec: 0.01-0.025 Ωcm Antimony (n) doped Silicon, 4 µm thick, tip spec: 10-15 µm height, 8 nm radius). RMS roughness (root mean square of the roughness), roughness average (R_a), and thickness of the films were analyzed using the WSXM software [121].

LEO (Zeiss) Gemini 1530 FEG-SEM was used for the acquisition of SEM images.

Sheet resistance (ρ_{sheet}) of CP films was determined using a **Jandel RM3000+ test unit** combined with a multi-height probe. Jandel 4 points cylindrical probe head with a tip radius of 500 µm was used.

Metrohm Autolab PGSTAT 101 and **IviumStat potentiostat** were used to record cyclic voltammograms (CVs) and electrochemical impedance spectra (EIS).

5 Characterization

5.1 Electronic band structure in CPs

In π-conjugated CPs with the backbone of sp^2 hybridized carbons, three valance electrons of carbon out of four form three sigma (σ) bonds, and one valance electron in p_z orbital orthogonal to the remaining three σ bonds participates in π-bonding with a neighbouring atom. In conjugated long-chain polymers, these closely located p orbitals allow the overlapping of molecular orbitals (MOs) to form π-bands. These bands form bonding (π) and anti-bonding (π*) bands which represent valance band (VB) and conduction band (CB), respectively. Generally, the delocalization of π-electrons through conjugated double bonds in CPs can be further increased by extending the conjugation length (**Figure 6**) [122].

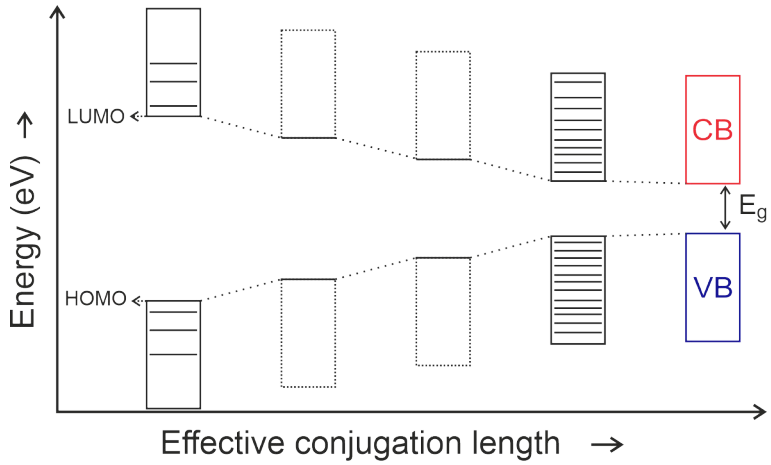

Figure 6. A schematic of band structure in CPs and effect of delocalization of π-electrons.

The increased delocalization of π-electrons occurs with a reduction in the energy gap between the highest occupied molecular orbital (HOMO) in VB and the lowest unoccupied molecular orbital (LUMO) in CB. This energy gap between HOMO and LUMO versus vacuum is called band gap (E_g), a tuneable property of CP. For insulators, the band gap is >8 eV, and conductivity is $<10^{-7}$ S/cm, whereas for conductors,

the bandgap is ~0 eV. In the case of CPs, the band gap is >3 eV, and conductivity is $<10^{-2}$ S/cm. This bandgap in CPs can be lowered to <3 eV, and conductivity can be increased to $>10^{-2}$ S/cm by the process called doping [123].

Bond length alternation in CPs: Peierls distortion [124] can be described as the geometrical distortion in which alternate bond length prefers localization of π-electrons favouring semiconductor type band structure in CPs, e.g., polyacetylene has a band gap of 1.5 eV and its alternate bond length prefer semiconducting state over metallic state. Chemical, photochemical, or electrochemical addition or elimination of electrons to/from the conjugated CP matrix generates charge carriers in the polymer backbone. This process of oxidation (p-doping) or reduction (n-doping) is called doping. It occurs with the formation of charge carriers such as soliton, polaron, bipolaron or polaron pairs in the polymer matrix [124–127]. Usually, the doping process raises the conductivity of CP and reduces the band gap by insertion of electronic states between VB and CB (**Figure 7**) [124–127]. Many additional factors also influence the bandgap of CPs, e.g., conformational changes, inter- and intrachain molecular interactions, conjugation length, substitution in polymer moieties, oxidant strength and properties of dopant ions, electrochemical switching potential, scan rate, and electrolyte solution for electrochemically synthesized CPs, etc.

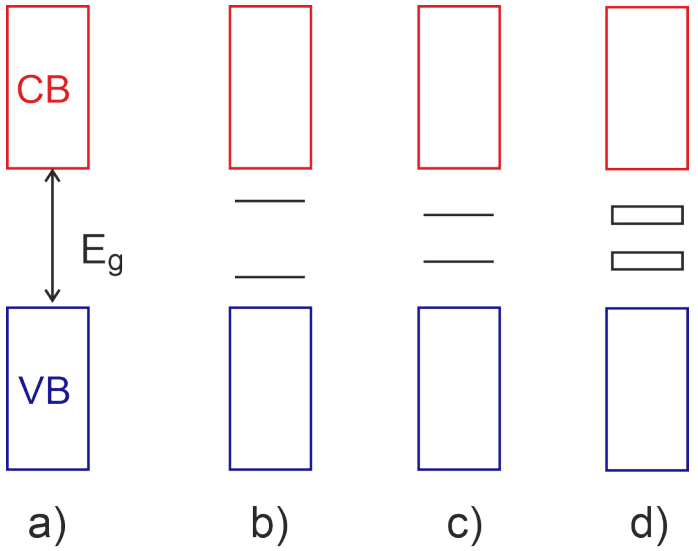

Figure 7. Band structure for CPs in a) neutral, b) polaron, c) bipolaron, and d) bipolaron band states.

5.2 Spectroscopic characterization

5.2.1 UV-Vis spectroscopy

Transmittance is an essential property of CP thin films for their applications in touchscreens, electronic displays, and smart windows. UV-Vis spectroscopy is an easy technique to determine the transmittance of the CP thin films. Transmittance change along with conductivity was monitored during the process-parameters optimization and layer-by-layer (L-b-L) deposition. Using UV-Vis spectra, the optical bandgap is determined with a tangential through the onset of the absorption spectrum. The transition between VB and CB as a result of doping can be observed using this technique. The π-π^* transitions and charge-carriers formation studied using UV-Vis spectra facilitated the comparison of the chemical nature of multi-layered CP films.

5.2.2 FTIR and Raman spectroscopy

IR (absorbance/ transmittance/ reflection) and Raman (scattering) spectra provide complementary information to each other. Vibrational transitions accompanied by a change in dipole moment are observed in IR spectra, and changes in polarizability are observed in Raman spectra. The counter ions doped during the polymerization process or forced doping along with additives (if used during the processes) can be detected using these techniques. In addition, the charge carrier formations in CP matrix during the doping process show absorbance in the NIR region.

5.2.3 In situ spectroelectrochemistry

In situ spectroelectrochemistry (in situ SEC) measurements allow simultaneous acquisition of spectroscopic data during the electrochemical measurements [82,95,128,129]. In situ SEC studies assist in understanding the chemical changes, interaction of dopant ions, and geometrical changes occurring in CPs during the electrochemical doping-dedoping experiments. For example, symmetric vibrational modes silent in the IR spectrum of a polyconjugated pristine polymer become polarised upon introducing charge carriers in the polymer backbone. It causes a break in the symmetry leading to doping-induced IR active vibrations (IRAV). Similarly, in situ UV-Vis-NIR spectroscopy can provide the associated change in optical bandgap, electronic transitions, and charge carriers' formation during the electrochemical doping-dedoping measurements. In situ SEC play an essential role in studying the reversibility of electrochemical redox processes of CPs.

An AP-VPP synthesized PEDOT film on a ZnSe hemisphere is used as a working electrode (WE) with Pt wire as a counter electrode (CE) and Ag/AgCl wire as a reference electrode (RE) for in situ ATR-FTIR spectroelectrochemical measurements (**Figure 8**). Similarly, an AP-VPP synthesized PEDOT film on FTO glass is used as the working electrode for in situ UV-Vis spectroelectrochemical measurements. **Figure 8** shows the schematic of both techniques with respective spectra. The cell design is given in the reference [82]. A reference spectrum is measured where no faradaic processes are observed in the CV. During the p-doping cycle, a spectrum was recorded at selected potential intervals. A spectrum calculated with 32 co-added interferograms covers a range of approximately 70 mV. The spectra were recorded using Harrick Seagull accessory with Bruker Vertex 70 spectrometer (liquid nitrogen cooled MCT detector). Spectra were collected at an incidence angle of 68° in a spectral range of 450 - 7000 cm^{-1} (4 cm^{-1} spectral resolution).

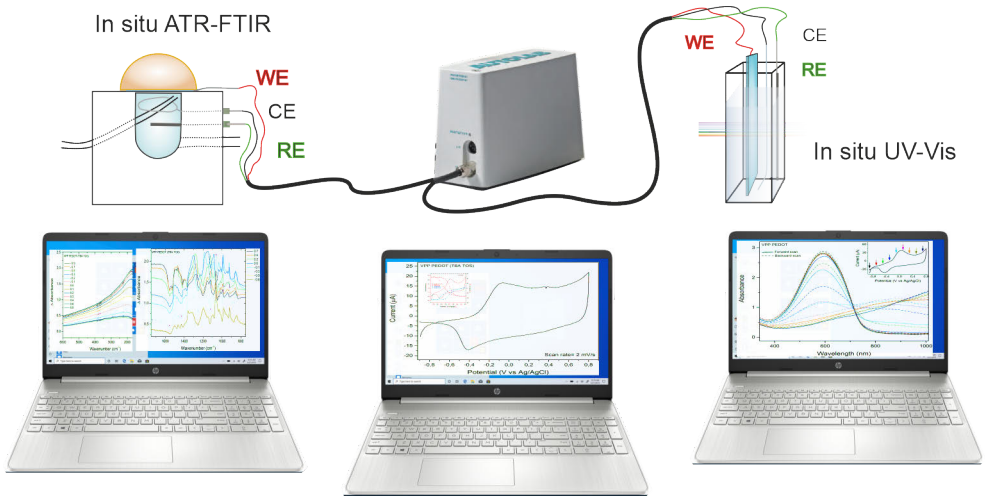

Figure 8. Schematic of in situ ATR-FTIR and in situ UV-Vis spectroelectrochemical measurements set-ups (built in-house).

5.3 Microstructural analysis

5.3.1 Optical microscopy

Basic features of CP thin film topography can be easily studied using well-known microscopic imaging techniques at a micrometre scale.

5.3.2 Atomic force microscopy

Gerd Binnig and Heinrich Rohrer were awarded the Noble prize in physics 1986 for their design of the scanning tunnelling microscope (STM) in 1981 [130]. The other half of this price was awarded to Ernst Ruska for his critical work in electron optics and the model of the first electron microscope [130]. Later on, G. Binnig and C.F. Quate invented atomic force microscopy (AFM), which combined the principle of STM and stylus profilometer [131]. An interaction between a sharp-tip-probe attached to a cantilever and a sample surface during the scanning causes bending in the cantilever due to the Van der Waals forces and additional chemical bonds and forces. This bending or deflection is investigated by using a laser beam reflecting from the back of the cantilever to a detector and further processed with the signals coming from the piezoelectric tube under the sample [131,132]. AFM is a powerful technique for analyzing CP thin film surface morphology at a nanometer scale.

5.3.3 Scanning electron microscopy

A short description about scanning electron microscopy (SEM) imaging technique has been put together using references [133–135]. A high energy electron beam of <10 nm size (compressed using lenses) penetrates (up to 1 μm), interacts, and scans a sample and the resulting signals are used to produce a SEM image of various magnifications. Backscattered electrons (BSE) and secondary electrons (SE) are primarily detected in this technique. BSEs are the result of an elastic collision of electrons with atoms giving scattered trajectories. In contrast, SEs originate from inelastic interaction between a primary electron beam and the surface region of the sample. SE images provide important topological/surface information. Whereas BSE (as coming from a deeper part) images are sensitive to atomic numbers and provide additional information about the crystallography. SEM imaging technique can come over the limitations faced by optical microscopy.

Effects of various method parameters on microstructures and surface properties of CP films are studied using AFM, SEM and microscope imaging. It provided complementary justifications for spectroscopic and electrochemical data analysis.

5.4 Electrical conductivity and electrochemical properties

5.4.1 Sheet resistance

Sheet resistance (ρ_{sheet}), also known as surface resistivity, is a measure of lateral resistance and property of thin films of semiconductors and conductors. The specific resistance (ρ) in 'Ω/sq' of a CP film is obtained by multiplying sheet resistance with

film thickness (s) in 'cm'. The thickness of the AP-VPP CP films was determined using AFM.

$$\rho = \rho_{sheet} \times s \quad (1)$$

The conductivity (σ in 'S/cm') is the inverse of its specific resistance (ρ).

$$\sigma = \frac{1}{\rho} \quad (2)$$

5.4.2 Cyclic voltammetry and electrochemical impedance spectroscopy

Cyclic voltammetry (CV) is an electrochemical technique for the analysis of redox reactions. It is a type of potentiodynamic technique where an applied potential is cycled between upper and lower switching potential at a specific scan rate. The current, potential, and time profiles are recorded using a potentiometer. CV is also a widely employed technique in the synthesis of CPs [126,127,136]. Electrochemical impedance spectroscopy (EIS) is a powerful technique used to analyze interfacial properties related to events occurring at the electrode surface. CV and EIS together are effective techniques in studying thin films of CP. In the present thesis, we utilized cyclic voltammetry to study redox behaviour, capacitance properties, doping-dedoping, reversibility, and effect of scan rate on multi-layered thin films of PEDOT and PAz.

Electrochemical impedance is measured by applying an excitation signal of a sinusoidal wave of alternating current (AC) voltage with different frequencies to an electrochemical cell, followed by measuring the pseudo linear response of AC current flowing through the cell [137,138]. EIS is an informative technique for extracting information on solution resistance, double-layer capacitance, diffusion-controlled processes, and rate/process of charge transfer in the polymer matrix. In the present thesis, EIS is used to interpret the cumulative effect of multiple layers of PEDOT on the potential dependent change in conductivity change and charge transfer resistance. Additionally, film thickness, diffusion-controlled current, and comparison of PEDOT deposited on bare glass and on ITO-coated glass supported understanding of the interfacial interaction in multi-layered PEDOT films

CV and EIS were conducted in a conventional 3-electrode configuration using a one-compartment Teflon cell specially designed for FTO glass and microscope glass substrates. PEDOT and PAz films on an FTO and microscope glass were used as working electrodes. Ag/AgCl and platinum wires were used as a pseudo reference and counter electrodes. The reference electrode was calibrated before and after every set of electrochemical measurements using a ferrocene redox couple. All solutions were purged with dry nitrogen gas for 15 min before measurement.

Charge (Q) is calculated by the integration current and time in a cyclic voltammogram. Areal and volumetric capacitances are calculated by using the following equations.

$$C_A = \frac{Q}{(\Delta V \times \mathrm{A})} \tag{3}$$

$$C_V = \frac{Q}{(\Delta V \times V)} \tag{4}$$

Where C_A is areal capacitance, C_V is volumetric capacitance, ΔV is the potential window, 'A' is the area of the electrode, and 'V' is the volume of the electrode.

6 Summary of results and discussion

Paper I details the optimized AP-VPP method for PEDOT and the effect of L-b-L synthesis on film properties. High conductivity thin films of PEDOT are produced using FeTOS as an oxidant and pyridine as a base inhibitor.

Paper II describes similar studies conducted for polyazulene with method parameter optimization. In addition, a comparison of AP-VPP synthesized PAz with electrochemically and chemically synthesized PAz is provided.

Paper III comprises studies on AP-VPP PAz films synthesized using various concentrations of $CuCl_2$, $CuBr_2$, $FeCl_3$, and FeTOS oxidants. The variations in the resulting film's morphologies, CVs, UV-Vis and FTIR absorption spectra are compared.

In all the three-listed publications, UV-Vis, FTIR and Raman spectroscopic analysis are utilized to understand the chemical nature, charge carrier formation in the polymer backbone, doped-state and associated quinoid/benzoid forms of the films. In addition, CV measurements are performed to compare their electroactivity, EIS measurements on PEDOT films reveal interfacial properties of multi-layered PEDOT films, and surface morphologies are studied using AFM and SEM analysis techniques.

Various method parameters studied in this work include oxidant (concentration and oxidant spin-coating rate), oxidant-film drying temperature, polymerization time, Oven/cell temperature, substrate temperature, annealing temperature, film-washing solvents, and drying under air/dry nitrogen gas stream. In the beginning, a vacuum oven was used as a polymerization chamber. Primarily the long polymerization times (over 30 mins) and low sheet resistance of synthesized PEDOT films motivated us to search for other synthesis alternatives. After that, the ultrasonic spray technique with a hot inert gas (such as nitrogen) assembly was used to prepare PEDOT films. This way of producing films acquired sheet resistance in non-conducting to MΩ/sq range and resulted in inhomogeneous film formation. A successful experimental trial of 'a beaker-in-beaker' placed on a hot plate and covered with a petri dish at atmospheric pressure produced much more homogeneous films with sheet resistance in kΩ/sq. In order to make the experimental set-up more practical and efficient, the AP-VPP cell was developed. Further improvement in oxidant

concentration, polymerization times, temperatures, and AP-VPP cell provided control over the properties of resulting films. The process parameters optimization and L-b-L synthesis led to high conductivity and high capacitance of PEDOT thin films. A brief summation of the influence of main method parameters, L-b-L synthesis on the film properties with additional results is summarized below.

6.1 Effect of AP-VPP method parameters on PEDOT film properties

6.1.1 Surface profile, roughness, and sheet resistance

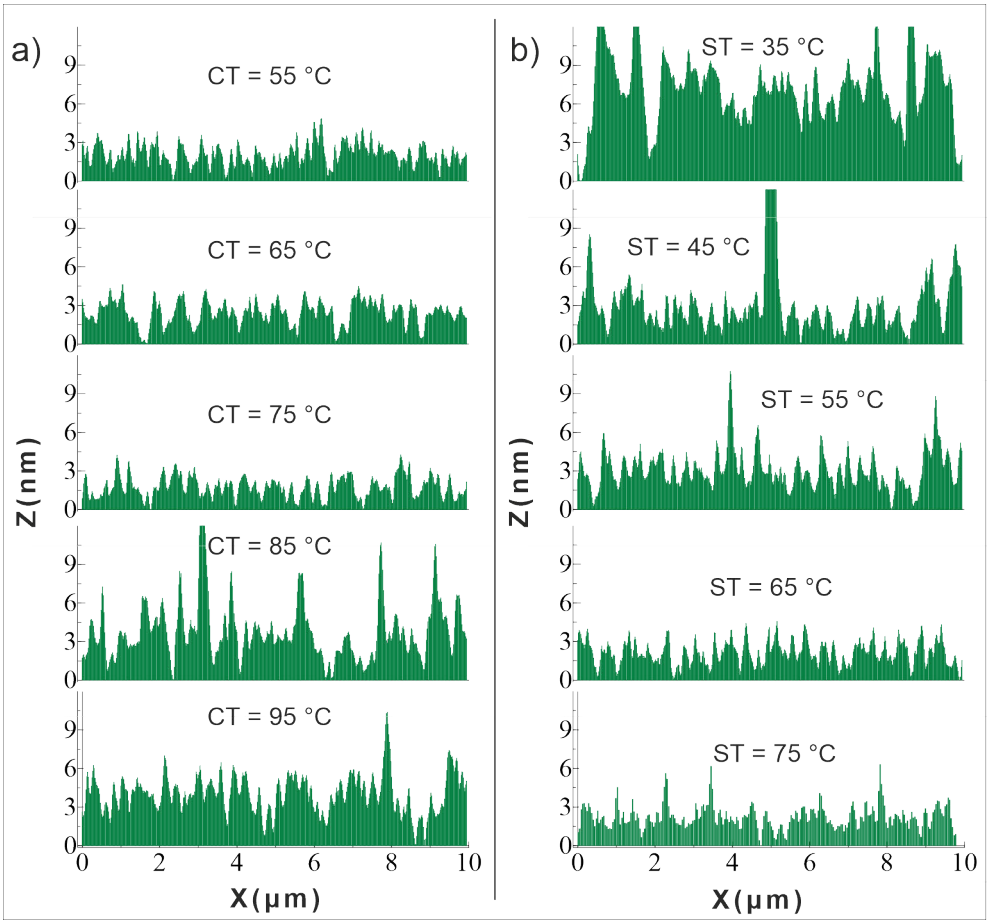

Figure 9. Surface profiles of PEDOT film synthesized on glass substrate at various **a)** cell temperatures (CTs) and **b)** substrate temperatures (STs). (Note: The ST was not controlled while testing the CT experiments, whereas CT was set at 75 °C while optimizing the ST).

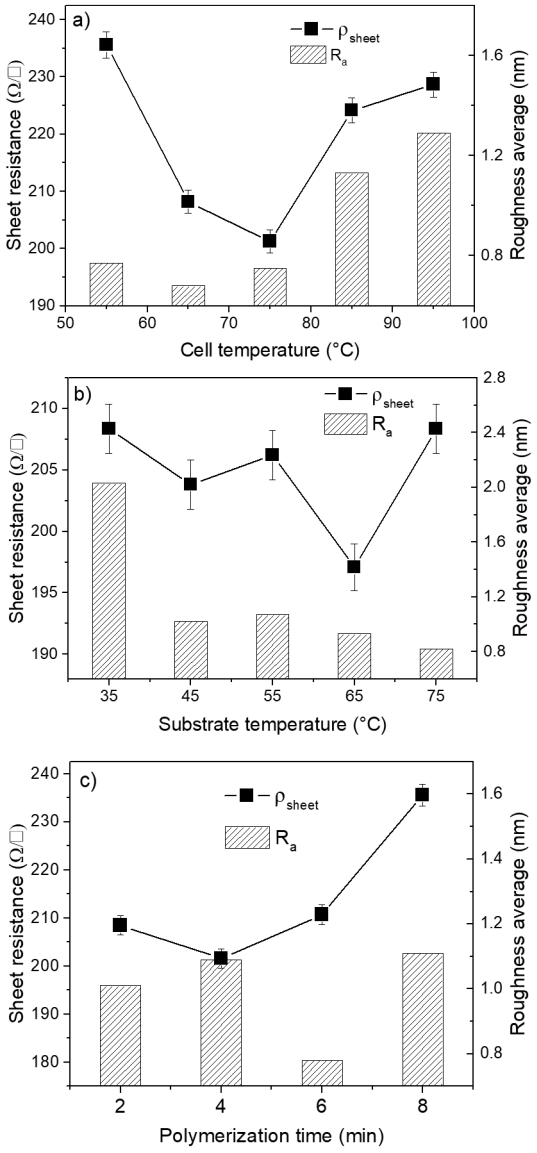

Figure 10. Sheet resistance (ρ_{sheet}) and roughness average (R_a) of PEDOT films synthesized at various **a)** CTs, **b)** STs, and **c)** polymerization times (PTs). (Note: CT was set at 75 °C while optimizing the PT)

The surface profiles shown in **Figure 9**a reveal that the PEDOT film's roughness average (R_a) increased with an increase in cell temperature (**Figure 9**a). Films produced at CT 65 and 75 °C attributed the property of uniformness; on the other hand, increasing substrate temperature (**Figure 9**b and **Figure 10**b) improved the smoothness of the films. This phenomenon, in both cases, results from condensation effects across the vapor concentration and temperature gradient and has been discussed in Paper I.

The sheet resistance (ρ_{sheet}) dropped with an increase in cell temperature until 75 °C; further increasing the cell temperature showed growth both in R_a and ρ_{sheet} values (**Figure 10**a). Similarly, the ρ_{sheet} dropped with an increase in substrate temperature until 65 °C and ascended with a further increase in substrate temperature. The polymerization time of 4 min among 2, 4, 6, and 8 min produced a film having low ρ_{sheet} (**Figure 10**c). Annealing films up to 60 °C did not lower the ρ_{sheet} significantly. However, the annealing between 70 to 90 °C lowered the ρ_{sheet} of PEDOT film by 8.3 %. ρ_{sheet} increased when films were annealed above 90 °C, implying PEDOT-degradation at high annealing temperature in air.

6.2 Effect of L-b-L synthesis on PEDOT film properties

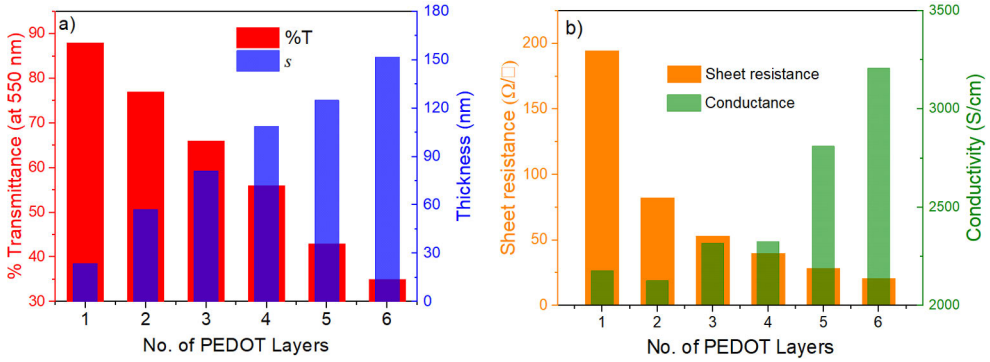

Figure 11. Trends in **a)** % transmittance (%T) and film thickness (s), and **b)** sheet resistance (ρ_{sheet}) and conductivity (σ) against the number of layers in PEDOT films synthesized on glass substrates.

6.2.1 % Transmittance and surface roughness

High %T and low R_a of 1L PEDOT make it a suitable candidate for optoelectronic applications. The AFM and SEM images of 1L to 6L PEDOT provided in Paper I show uniformness in the films. The R_a does not surpass 1 nm for 1L and 4 nm for 6L PEDOT, showing minimal growth in surface roughness with the addition of layers. An increase in thickness with the addition of layers and a fairly linear decline in %T can be observed in **Figure 11**a.

6.2.2 Sheet resistance, film thickness, and Conductivity

The multi-layered PEDOT films prepared using the optimum concentration of oxidant FeTOS and base inhibitor Py showed a closely packed arrangement of large conductive domains and improved in-plane conductivity. The interfacial growth of PEDOT at the oxidant and monomer-vapor interface limits the access of the tosylate dopant anion to the surface of the oxidant layer. The L-b-L synthesis ensures the new interface for each layer in multi-layered PEDOT film, confirming dopant anion availability across the multi-layered film. With the addition of layers, the sheet resistance decreases from 195 Ω/sq for 1L PEDOT to 21 Ω/sq for 6L PEDOT, while the conductivity and thickness keep increasing (**Figure 11**a and b).

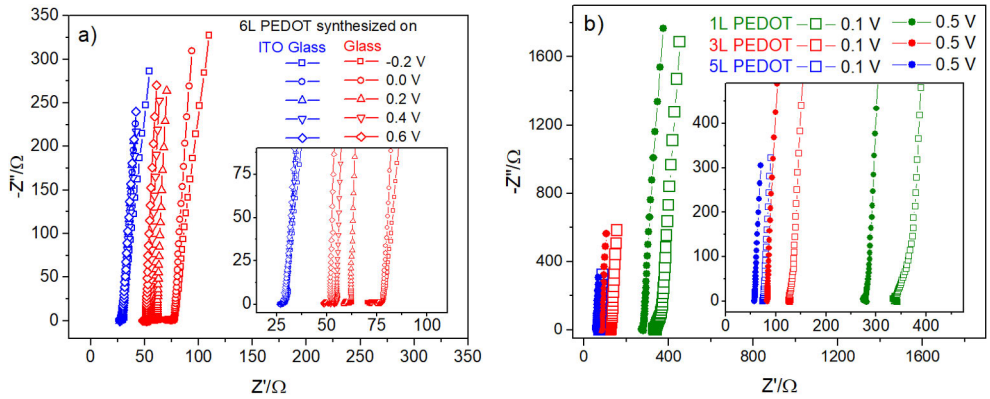

Figure 12. Nyquist plot of electrochemical impedance spectra (EIS) of a) 6L PEDOT prepared on glass and ITO glass (at−0.2, 0.0, 0.2, 0.4, and 0.6 V), and b)1L, 3L, and 6L of PEDOT on glass measured at 0.1 and 0.5 V.

Figure 12a compares the EIS spectra of PEDOT with and without the current collector electrode. The shifts in charge transfer resistance (CTR) of 6L PEDOT at applied potentials between -0.2 to 0.6 V do not occur on ITO glass (as a current collector). The reduction in CTR of PEDOT/glass at higher applied electrochemical potentials demonstrates improved conductivity of PEDOT as a function of doping. In **Figure 12**b, the clearly visible drop in CTR shows the significantly improved conductivity of the films with the addition of layers. These improvements are visible at both the measurement potentials of 0.1 V and 0.5 V. Another observation in **Figure 12**b is that the magnitude of CTR drop between 0.1 and 0.5 V shrinks with the addition of layers, proving refinement in the doped native form of the films and conductivities. It also explains why the fill factor (obtained from CVs in Paper I) improves from 83.3 % for 1L to 84.5 % for 3L and 86.1 % for 6L PEDOT. The high areal (10.7 mF/cm^2) and volumetric capacitance (704 F/cm^3) of 6L PEDOT signify the use of organic material for energy conservation.

6.2.3 Charge carriers and extended conjugation

As reported in Paper I, the increased absorbance of charge carriers formations (polaron/polaron pairs/bipolarons) above 650 nm and in the NIR region with the addition of PEDOT layers, and redshift in the spectra reveal the improved inter and intrachain interactions in the polymer matrix. Furthermore, it shows that adding PEDOT layers enhances charge mobility and justifies the high conductive phase in multilayered PEDOT films. The IR spectra, in situ SEC measurements, and Raman spectra unveil the extended conjugation and quinoid forms in the AP-VPP synthesized PEDOT films. The in situ IR spectra of PEDOT at -0.9 (neutral) and 0.5 V (p-doped)

are compared with the IR spectrum of 6L PEDOT. The blue shift of C_α=C_β, and red shift of C_α-C_α, and C_β-C_β, bands, along with shrinking in oxyethylene ring bending vibrations of doped PEDOT compared to the neutral form, is a result of extended conjugation. The inflow of bulky TOS^- dopant anions to counterbalance the charge development in the film must have seized bending vibrations of oxyethylene ring due to the crowding effect. The comparison of 6L PEDOT with in situ IR analysis of doped and neutral PEDOT (described in Paper I) reveals its doped form and extended conjugation in the polymer matrix. Additionally, improved conductivities, reduced CTR and ρ_{sheet}, and the redshift of C_α-C_β(-O) stretching vibrations from 2L to 6L PEDOT observed in Raman spectra propose the advancing quinoid form of the PEDOT films with the addition of layers.

6.3 Effect of AP-VPP method parameters on PAz film properties

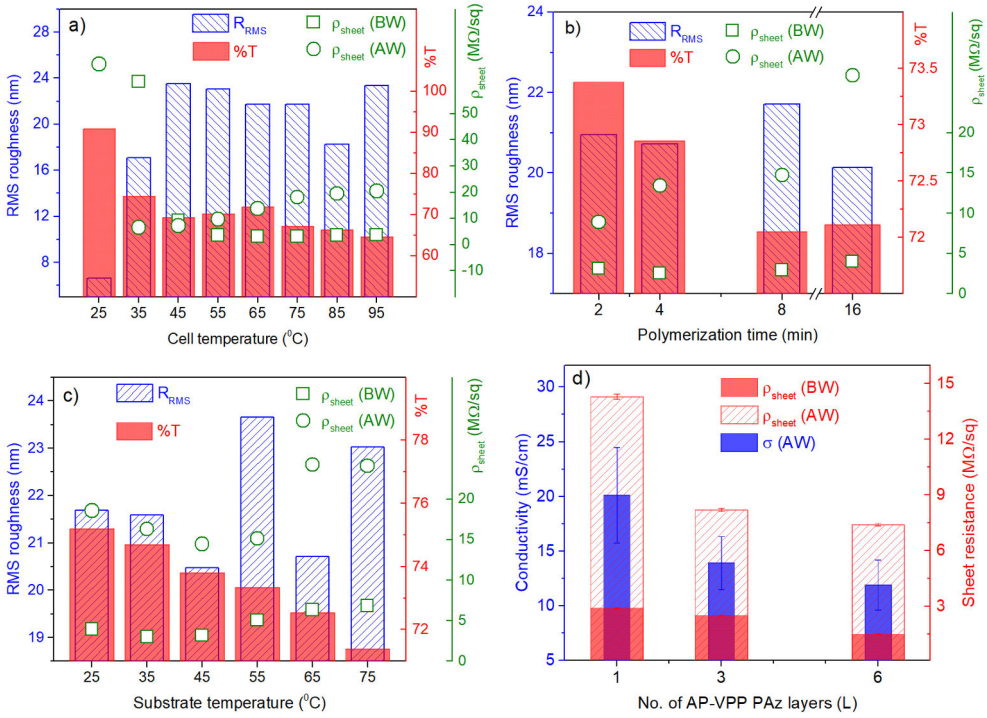

Figure 13. Surface roughness (R_{RMS}), %T (at 550 nm), and ρ_{sheet} before and after washing (BW and AW) of PAz films synthesized at various **a)** CTs, **b)** PTs, and **c)** STs. (Note: CT was set at 57 °C while optimizing the PT and ST). **d)** σ and ρ_{sheet} (BW and AW) of 1L, 3L and 6L PAz films.

A polymerization time of 4 min was used while optimizing CT and ST. CT of 57 ◦C was applied while optimizing PT and ST. ST control was removed during CT and PT optimization experiments. All the PAz films reported in the present section (section 6.3) are synthesized using 240 mM of $CuCl_2$. Abbreviations AW and BW are used to show the effect of before and after washing films on sheet resistance of the films. All other film characterizations are performed after washing the films as defined in the general procedure given in section 3.1.

6.3.1 Roughness, sheet resistance and % transmittance

In **Figure 13**a, at 25 °C of CT, ρ_{sheet} (BW) did not exhibit any value and ρ_{sheet} (AW) was very high. Additionally, high % T and R_{RMS} prove thin and poor film deposition, which is further discussed in Paper II. In **Figure 13**a, trend reversal after 45 °C of CT can be observed for ρ_{sheet} (BW and AW) and R_{RMS}. The increasing surface roughness with CT starts diminishing after 45 °C of CT until 85 °C and raises up at 95 °C. Similarly, ρ_{sheet} dropped after washing the film until 45 °C, this trend shows reversal after 45 °C of CT. Overall, % T keeps dropping with CT except at 55 and 65 °C. Optical bandgap estimations of these films are provided in Paper II. These trends in properties of PAz films with change in CT are described in Paper II by using the phenomena of fast deposition and elevated polymerization rate induced cross polymerization.

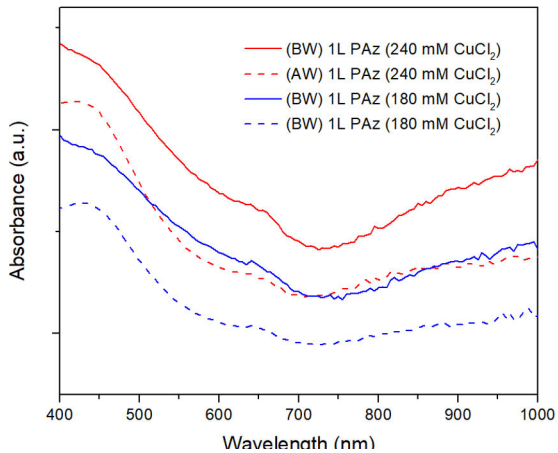

Figure 14. UV-Vis spectra of (BW) and (AW) 1L PAZ (180 mM and 240 mM $CuCl_2$).

In **Figure 14**, the decrease in absorbance around 450 nm (π-π* transition in the neutral part of PAz) and an even more decrease in absorbance above 800 nm (absorption by charge carriers' formation) indicate the loss of soluble oligomers during the washing process. The drop in ρ_{sheet} after washing of the film must be due to the loss of soluble high conductivity oligomers.

Similarly, a washing effect on ρ_{sheet} can be observed in **Figure 13**b and c for polymerization time and substrate temperature experiments. Reduced transmittance of PAz film synthesized using 8 and 16 min of PT compared to 2 and 4 min could be due to the additional polymer deposition. The extended conjugation with increase in PT from 2 min to 4 and 8 min is supported by

a reduction in the optical bandgap of PAz films. The high conductivity of short-chain PAz demonstrates why ρ_{sheet} (AW) increases with PT.

All the trends in **Figure 13**c are justified in Paper II by realizing the fast deposition at elevated temperature, and simultaneous temperature gradient (between substrate and monomer vapor) influenced condensation. **Figure 13**c shows the falling % T and R_{RMS} (except zigzag growth at 55 to 75 °C) with increasing ST. Furthermore, ρ_{sheet} (BW) drops slightly till 45 °C and continues to rise slightly till 75 °C, whereas ρ_{sheet} (AW) drops till 45 °C, slightly rises at 55 °C, and considerably rises at 65 °C, and stay almost constant at 75 °C. It can be summarized as the trends in % T and R_{RMS} are caused by a diminished overall film deposition due to slow or restricted inflow of monomer vapor with the increase in ST and concurrently occurring elevated rate of polymerization triggered aggregates. The increase in the optical bandgap of the films from 25 to 55 °C of ST remains constant at 65 and 75 °C. It supports the above justification, as the limited monomer inflow and increased rate of polymerization would lead to short chain polymers dropped ρ_{sheet} and ST above 55 °C would lead to a cross-linked-polymer caused increase in ρ_{sheet}.

6.4 Effect of L-b-L synthesis on PAz film properties

6.4.1 Conductivity and sheet resistance

The increase in absorbance around 450 nm (arising from a neutral part of the polymer) and 660 nm (owing to the charge carriers generation upon doping) in UV-Vis spectra reported in Paper II reveals that the PAz film produced by AP-VPP is in a partially doped state. Increased absorbance with the addition of layers is observed in UV-Vis spectra. The absorbance bands in NIR spectra (Paper II) suggest the radical cation formations in the PAz films. The red shift observed with the addition of layers and the shrinking optical bandgaps from 1L to 3L and to 6L PAz could be the synergistic influence of increasing azulene units in polymer chains and suggests the extended delocalization of the charge across the multiple layers. The overall amount of doping reduces with the addition of layers. The enhancement in charge delocalization concurrently with the reduction in doping degree suggests more planar than distorted nonplanar conformation in PAz with the addition of layers. The drop in ρ_{sheet} can be seen in **Figure 13**d. The reduction in conductivity with the growing number of layers must be attributable to the non-linear and insufficient drop in sheet resistance. The effect of washing on ρ_{sheet} observed in **Figure 13**d could be due to the loss of soluble oligomers.

6.4.2 Areal and volumetric capacitance

The enhanced current densities with scan rate can be observed in the CVs of 1L, 3L, and 6L PAz reported in Paper II. The highest current density in the CV of 6L PAz demonstrates the influence of adding electroactive PAz layers. As noticeable from the CVs, the areal capacitance grows from 1L to 6L PAz (**Figure 15** a). In **Figure 15** a and b, the C_A and C_V of 1L remains relatively constant at different scan rate from 50 to 200 mV/s signifying unaffected diffusion-controlled processes at high scan rate. Comparatively, these processes are a little impacted in 3L PAz, and further in 6L PAz. The reason can be explained by the drop in conductivity and closely-packed array of island structures (revealed in AFM and SEM images in Paper II) with L-b-L growth. C_A and C_V of 8.3 ± 0.31 mF/cm^2 and 706.2 ± 140.3 F/cm^3 of 6L PAz at 20 mV/s scan rate imply AP-VPP PAz as a potential material for energy storage applications.

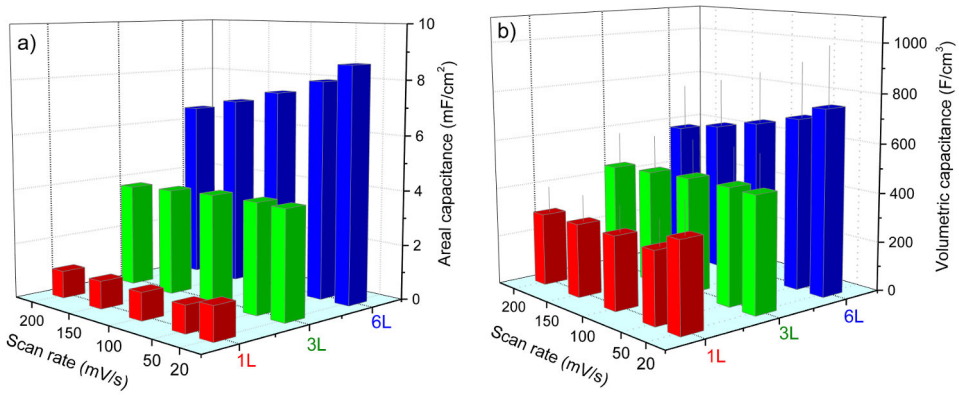

Figure 15. a) Areal and **b)** volumetric capacitances of 1L, 3L, and 6L PAz against scan rate.

6.5 Effect of oxidant on properties of PAz films

6.5.1 Surface morphologies

Comprehensive discussion and additional microscope and AFM images are provided in Paper III.

All four oxidants ($FeCl_3$, $CuBr_2$, $CuCl_2$, and FeTOS) used to synthesize PAz films by AP-VPP produced discrete morphologies in 1L and 3L PAz films (**Figure 16** and **Figure 17**). PAz films synthesized using 60 mM of $FeCl_3$ formed poor-quality films, and an increase in the concentration to 120 mM enhanced the connecting island structures. Crowding of these structures was observed with the addition of layers. The $CuBr_2$ synthesized films formed more scratchy and rough patches than the

connecting island structures. The crowding-connecting effect among the PAz island structures and size distribution was observed as a result of increased concentration to 120 mM and multiple layers. PAz films of well-ordered microstructures were produced using $CuCl_2$ oxidant. Increasing the concentration of $CuCl_2$ from 60 to 240 mM caused the assembling and filling of grainy porous structures. PAz films (partially doped with bulky tosylate ions), when synthesized using FeTOS, showed stress-induced ruptures during the washing process. As a result, broken and overlapped pieces became complex and orbicular with the increasing concentration from 60 to 240 mM of FeTOS and with the addition of layers.

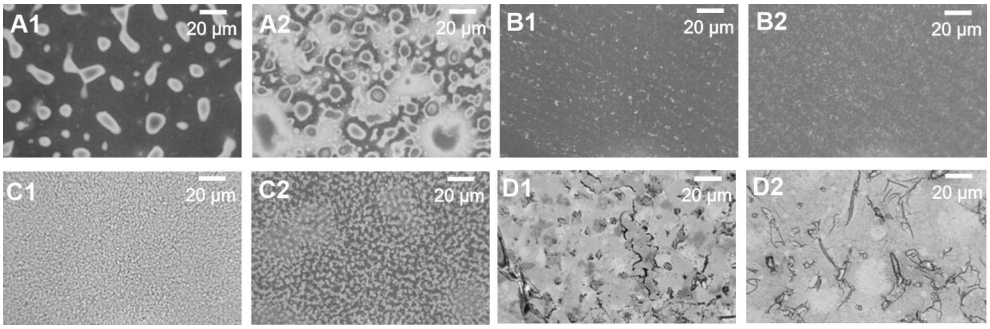

Figure 16. Microscope images of 3L PAz **A1)** (60 mM $FeCl_3$), **A2)** (120 mM $FeCl_3$), **B1)** (60 mM $CuBr_2$), **B2)** (120 mM $CuBr_2$), **C1)** (60 mM $CuCl_2$), **C2)** (120 mM $CuCl_2$), **D1)** (60 mM FeTOS), **D2)** (120 mM FeTOS).

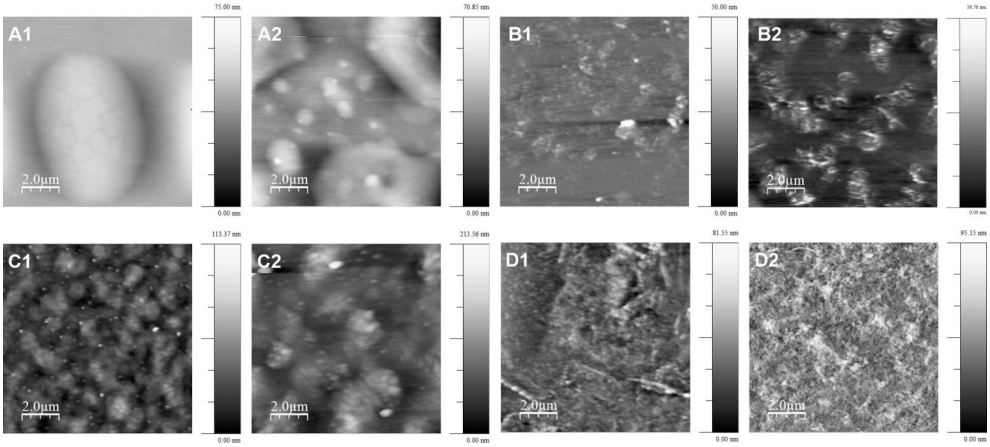

Figure 17. AFM images (10 × 10 µm) of 3L PAz **A1)** (60 mM FeCl3), **A2)** (120 mM FeCl3), **B1)** (60 mM $CuBr_2$), **B2)** (120 mM $CuBr_2$), **C1)** (60 mM $CuCl_2$), **C2)** (120 mM $CuCl_2$), **D1)** (60 mM FeTOS), **D2)** (120 mM FeTOS).

6.5.2 Phase segregations

PAz films showed a pre-peak before the main oxidation peak in their CVs. The appearance and shape of prepeaks changed depending on multiple PAz layers in the film and the type and concentration of oxidant used in the synthesis. All the pre-peaks were analysed in paper III and revealed insights into film properties. The CVs of 3L PAz (60 mM $CuCl_2$) and 1L PAz (120 mM $CuCl_2$) exhibited single pre-peak formation, whereas 3L PAz (120 mM $CuCl_2$) showed a single pre-peak at higher scan rates except for slight peak splitting at 50 mV/s. Similarly, splitting was observed in CVs of 1L PAz (180 mM $CuCl_2$) at 50 and 100 mV/s, whereas it was noticed at all scan rates for 3L PAz (180 mM) and 1L and 3L PAz (240 mM $CuCl_2$). It is slightly visible at 20 mV/s in CVs of 1L PAz (120 mM $CuBr_2$), whereas noticeable until 150 mV/s for 3L PAz (120 mM $CuBr_2$). CVs of 3L PAz (60 mM) and 1L PAz (120 mM FeTOS) contained single pre-peak at 20 and 50 mV/s scan rate, whereas 3L PAz (120 mM FeTOS) showed pre-peak splitting at 20 mV/s. No current peaks were observed in CVs of 1L and 3L (180 and 240 mM FeTOS).

These studies indicate the splitting dominancy at low scan rates in 3L films synthesized using high oxidant concentrations. Higher oxidant concentrations and multiple layers possibly result in thicker films and phase separation. At a slow scan rate, these phases reveal individual appearances in CVs. The compact sheets and broken-overlapped orbicular structures that restricted ion penetration and doping-induced geometrical changes for charge compensation can explain the poor electrochemical performance of FeTOS synthesized films.

6.5.3 UV-Vis spectra

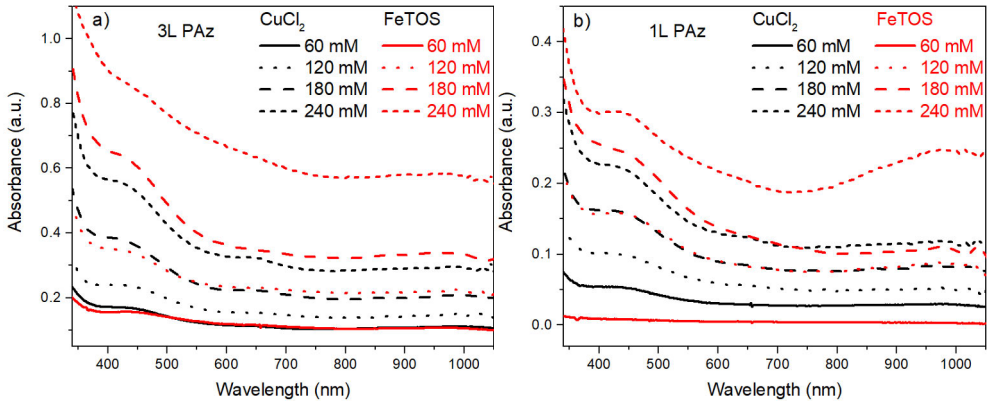

Figure 18. UV-Vis spectra of **a)** 3L PAz and **b)** 1L PAz (60, 120, 180, and 240 mM $CuCl_2$) and (60, 120, 180, and 240 mM FeTOS).

An absorption band centered around 450 nm in UV-Vis spectra of PAz films arises from absorption due to π-π* transition in the neutral part of PAz. In addition, a shoulder appearing around 660 nm (and beyond) is because of the absorption by charge carriers' generation (polarons/bipolarons/polaron pairs) upon doping of the film.

The enhanced deposition of PAz with increasing concentration of $CuCl_2$ and FeTOS can be observed in the absorbance due to the neutral part of PAz in UV-Vis spectra reported in Paper III. In contrast, it is not as significant as the other two with the concentration of $FeCl_3$ and $CuBr_2$. The absorbance comparison at 450 and 640 nm shows the less doped form of $CuBr_2$ synthesized PAz films than $FeCl_3$. A similar comparison for $CuCl_2$ reveals the dominating absorbance due to the neutral form over the doped form of the film with increasing concentration (**Figure 18** a and b). In contrast, a high concentration of FeTOS exhibited proportional absorbances. The comparison between $CuCl_2$ and FeTOS revealed that FeTOS produced highly oxidized PAz films.

6.5.4 FTIR spectra

The FTIR spectra of PAz in the NIR region show absorption due to chemical or electrochemical doping-induced charge carriers formation in the film matrix. The comparison of absorption bands observed in this region and fingerprint region for various PAz films and their further comparison with available literature is provided in Paper II and III.

In **Figure 19**a, the radical dications dominated NIR spectra of various concentrations of $CuCl_2$ synthesized films indicate a medium doping level of all films. Furthermore, the red shift (6670 to 5995 cm^{-1}) in absorbance due to the formation of radical dications with increasing concentration of $CuCl_2$ indicates the reduced conjugation in PAz films. In the NIR region (**Figure 19**b), the red shift in radical dications absorbance (6290 to 5337 $cm^{-1)}$ and blue shift (3300 to 4224 cm^{-1}) in radical cations absorbance with increasing concentration of FeTOS suggest a trend of reduced conjugation length in resulting PAz films. The significant shift at a high concentration of FeTOS indicates some drastic change in PAz films. Similarly, drastic changes are also noticed in morphologies, UV-Vis spectra, and cyclic voltammograms of these films at high concentrations (180 and 240 mM) of FeTOS. The spectra of radical cation and dication formations suggest a medium doping level for 3L (60 and 120 mM FeTOS), whereas a low to medium level for 3L (180 and 240 mM FeTOS). The comparison of broad absorption maxima in the NIR region shown by PAz films reveals that the order of doping level is highest in 3L PAz (120 mM FeTOS) followed by 3L PAz (120 mM $FeCl_3$) > 3L PAz (120 mM $CuCl_2$) and lowest in 3L PAz (120 mM $CuBr_2$). The intensity of IRAV bands are reported in Paper III, which supports this order.

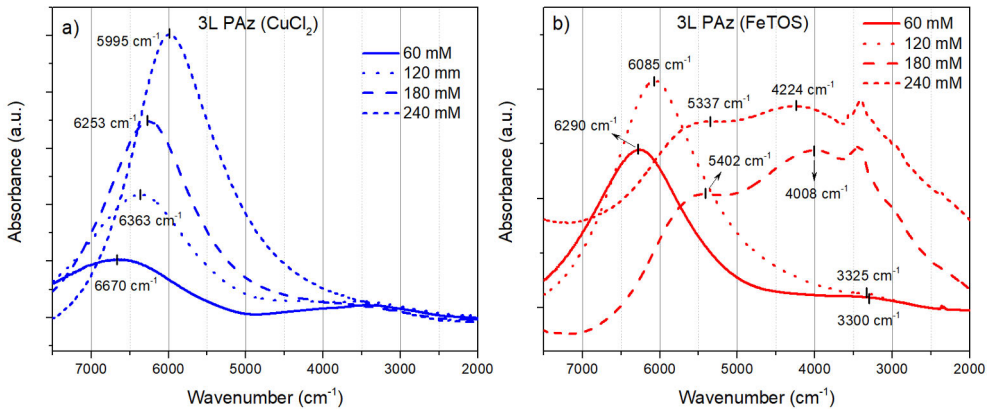

Figure 19. FTIR spectra of **a)** 3L PAz (60, 120, 180, and 240 mM $CuCl_2$) and **b)** 3L PAz (60, 120, 180, and 240 mM FeTOS) in the range 7500 to 2000 cm^{-1}.

7 Conclusions and closing remarks

With the help of available literature on PEDOT, the thesis work aimed to develop and optimize a robust VPP process at atmospheric pressure to fabricate PEDOT and PAz thin films on desired substrates in simple and cost-effective ways. In addition, it also focused on PEDOT as an effective organic alternative to ITO.

In this thesis, ultra-thin electroactive films of both PEDOT and PAz are successfully synthesized using our developed and optimized AP-VPP process. Furthermore, the process parameters can be tuned to alter the properties of both the studied CPs. The L-b-L synthesis using optimized AP-VPP provided the engineering ability for CP thin film at a thickness scale of nanometers. In addition, improved conductivities for PEDOT and capacitance for PAz and PEDOT are also obtained using the L-b-L synthesis approach. The conformational changes traced using spectroscopic characterization techniques facilitated the comparison between CP films of multiple layers and provided insights into inter/intra chain interactions upon doping.

Apart from the properties of monomer unit, the chemistry of AP-VPP CP thin films properties mainly revolves around conjugation length in resulting films, doping degree, the redox nature of charge carriers formed upon doping-dedoping, surface properties of deposition-substrate, solvents used for oxidant/oxidant-inhibitor solution and washing, type and stoichiometry of oxidant, rate and time of polymerization, temperature of cell and substrate, annealing temperatures, and properties of dopant ions. In addition, influences on the order of nano- to microstructures in morphologies play an essential role in determining the overall properties of the resulting CP film.

The high conductivity, very low surface roughness, stability in the air, and high transmittance of 1L to 6L PEDOT films produced in the present thesis work encourage their application in energy storage devices and as transparent electrodes for touchscreens and bendable devices. 15L PEDOT film and composites with reduced graphene oxide were synthesized in order to increase the capacitance density. The simple capacitive mono-touch bendable prototype prepared in this work shows a proof-of-concept study for touch screen applications. Besides, the biocompatibility of AP-VPP PEDOT films preceded their ongoing application in bio-photovoltaic devices. Moreover, ongoing applications include AP-VPP PEDOT on cellulose in green piezoelectric sensors, in sensors integrated with wearable and washable fabrics

and in electrochromic smart windows. The challenge of large surface area application has been partially overcome through successful scale-up to the area of 484 cm^2 at lab premises. However, the challenge of organic material stability at high lamination temperatures in already developed infrastructure for ITO and harsh environmental stability tests remain as obstacles, though the device-encapsulated stability tests are not yet performed. One solution could be the development of protective layers of primers to increase stability or infrastructure optimization according to the compatibility of organic materials.

Acknowledgement

I thank the Materials Chemistry Research Group and the Chemistry Department at the University of Turku for letting me conduct PhD studies. Furthermore, I express my gratitude towards the University of Turku and the Doctoral Programme in Exact Sciences (EXACTUS). I am grateful to the Real Estate Foundation, Fortum Foundation, Jenny and Antti Wihuri Foundation, Business Finland, and the University of Turku for the financial support.

I thank Carita for giving me the opportunity to perform PhD studies. I also thank her for providing a platform full of opportunities, freedom in research, and continuous support and care. I thank her for providing education and guidance and writing reference letters for all my funding applications. I thank Prof. Santosh Haram and Bhushan Gadgil for bringing the knowledge of the opportunity to me.

I thank Pia for her continuous guidance, support, education, and training. In addition, I thank Pia for writing reference letters for all my funding applications and keeping labs and instruments in order and functional. You are my best friend and future collaborator. All the designs and works were possible because of Pia and Mauri.

I thank Milla for all her help, education, and friendship. I thank Lokesh for his words of wisdom and friendship. I thank Anssi and the team for IP rights and COMPOL. I thank Mauri for all the technical support, Kirsi for all the chemicals and orders, and Kari for taking care of the computers and software. Without you three, we cannot work smoothly. I thank all the heads of the chemistry department and administrative staff for smooth document processing during the journey.

I thank Prof. Krzysztof Winkler and A. Prof. Trisha Andrew for reviewing my thesis. I thank A. Prof. Anna Maria Coclite for accepting the responsibility of the opponent's position.

I thank Ari and Harri, I always enjoy our short communications. Life is colourful with friends. I thank my labmates, colleagues, and friends Mikko, Sachin, Vijay, Ajit, Nianxing, Adefunke, Jenna, Ashwini, Jesse, Bo, Madhu, György, Tommi, Atte, Mia, Ibrahim, Felix, Emilia, Isabella, Lauri, Hellen, Natalia, Minea, Hannah, Sami, Tharun, Plawan, Sajal, and Narhari for sharing the joyful moments. I thank Santosh, Preeti, Kedar, Renuka, Satish, Swathi, Senthil, Ameya, Rahul, Ankitha, Joakim, Bishwesvar, and all my friends in India.

I thank all the teachers from my birth till this point and future guides. I am always grateful to you all.

I thank my mother, Shakuntala, for being everything to me. I thank my brother Mangesh and sister Sonali and their families for being integral to my life. Three of you and all associated with you are important to me.

November 2022
Rahul Yewale

References

[1] Y. Huang, E.L. Hsiang, M.Y. Deng, S.T. Wu, Mini-LED, Micro-LED and OLED displays: present status and future perspectives, Light Sci Appl. 9 (2020). https://doi.org/10.1038/S41377-020-0341-9.

[2] B. Geffroy, P. le Roy, C. Prat, Organic light-emitting diode (OLED) technology: Materials, devices and display technologies, Polym Int. 55 (2006) 572–582. https://doi.org/10.1002/PI.1974.

[3] H.W. Chen, J.H. Lee, B.Y. Lin, S. Chen, S.T. Wu, Liquid crystal display and organic light-emitting diode display: present status and future perspectives, Light Sci Appl. 7 (2018) 17168. https://doi.org/10.1038/LSA.2017.168.

[4] A.D. Arnold, P.E. Castro, T.K. Hatwar, M. v. Hettel, P.J. Kane, J.E. Ludwicki, M.E. Miller, M.J. Murdoch, J.P. Spindler, S.A. van Slyke, K. Mameno, R. Nishikawa, T. Omura, S. Matsumoto, Full-color AMOLED with RGBW pixel pattern, J Soc Inf Disp. 13 (2005) 525. https://doi.org/10.1889/1.1974009.

[5] D.H. Kim, Y.J. Lim, D.E. Kim, H. Ren, S.H. Ahn, S.H. Lee, Past, present, and future of fringe-field switching-liquid crystal display, Journal of Information Display. 15 (2014) 99–106. https://doi.org/10.1080/15980316.2014.914982.

[6] J.A. Castellano, Liquid crystal display applications past, present & future, Liquid Crystals Today. 1 (1991) 4–6. https://doi.org/10.1080/13583149108628568.

[7] V.W. Lee, N. Twu, I. Kymissis, Micro-LED technologies and applications, Inf Disp (1975). 32 (2016) 16–23. https://doi.org/10.1002/J.2637-496X.2016.TB00949.X.

[8] H. Nam, K.H. Seol, J. Lee, H. Cho, S.W. Jung, Review of Capacitive Touchscreen Technologies: Overview, Research Trends, and Machine Learning Approaches, Sensors 2021, Vol. 21, Page 4776. 21 (2021) 4776. https://doi.org/10.3390/S21144776.

[9] K. Reynolds, P. Shepelev, A. Graf, 46-1: Invited Paper: Touch and Display Integration with Force, SID Symposium Digest of Technical Papers. 47 (2016) 617–620. https://doi.org/10.1002/sdtp.10763.

[10] G. Walker, M. Fihn, LCD in-cell touch, Inf Disp (1975). 26 (2010) 8–14. https://doi.org/10.1002/J.2637-496X.2010.TB00228.X.

[11] H. Li, Y. Wei, H. Li, S. Young, D. Convey, J. Lewis, P. Maniar, 32.5L: Late-News Paper: Multitouch Pixilated Force Sensing Touch Screen, SID Symposium Digest of Technical Papers. 40 (2009) 455. https://doi.org/10.1889/1.3256814.

[12] H.K. Kim, S. Lee, K.S. Yun, Capacitive tactile sensor array for touch screen application, Sens Actuators A Phys. 165 (2011) 2–7. https://doi.org/10.1016/J.SNA.2009.12.031.

[13] G. Walker, A review of technologies for sensing contact location on the surface of a display, J Soc Inf Disp. 20 (2012) 413–440. https://doi.org/10.1002/jsid.100.

[14] W. Jing, C.H. Lai, S.H.W. Wong, M.L.D. Wong, Battery-supercapacitor hybrid energy storage system in standalone DC microgrids: Areview, IET Renewable Power Generation. 11 (2017) 461–469. https://doi.org/10.1049/IET-RPG.2016.0500.

[15] M. Şahin, F. Blaabjerg, A. Sangwongwanich, A Comprehensive Review on Supercapacitor Applications and Developments, Energies (Basel). 15 (2022) 674. https://doi.org/10.3390/en15030674.

[16] D.P. Chatterjee, A.K. Nandi, A review on the recent advances in hybrid supercapacitors, J Mater Chem A Mater. 9 (2021) 15880–15918. https://doi.org/10.1039/D1TA02505H.
[17] S. Pohlmann, Metrics and methods for moving from research to innovation in energy storage, Nat Commun. 13 (2022). https://doi.org/10.1038/s41467-022-29257-w.
[18] J. Sun, B. Luo, H. Li, A Review on the Conventional Capacitors, Supercapacitors, and Emerging Hybrid Ion Capacitors: Past, Present, and Future, Advanced Energy and Sustainability Research. (2022) 2100191. https://doi.org/10.1002/aesr.202100191.
[19] M. Kolokotroni, X. Ren, M. Davies, A. Mavrogianni, London's urban heat island: Impact on current and future energy consumption in office buildings, Energy Build. 47 (2012) 302–311. https://doi.org/10.1016/J.ENBUILD.2011.12.019.
[20] M. Brzezicki, A systematic review of the most recent concepts in smart windows technologies with a focus on electrochromics, Sustainability (Switzerland). 13 (2021) 9604. https://doi.org/10.3390/SU13179604/S1.
[21] Y. Ke, J. Chen, G. Lin, S. Wang, Y. Zhou, J. Yin, P.S. Lee, Y. Long, Smart Windows: Electro-, Thermo-, Mechano-, Photochromics, and Beyond, Adv Energy Mater. 9 (2019) 1902066. https://doi.org/10.1002/aenm.201902066.
[22] M. Casini, Active dynamic windows for buildings: A review, Renew Energy. 119 (2018) 923–934. https://doi.org/10.1016/j.renene.2017.12.049.
[23] R. Tällberg, B.P. Jelle, R. Loonen, T. Gao, M. Hamdy, Comparison of the energy saving potential of adaptive and controllable smart windows: A state-of-the-art review and simulation studies of thermochromic, photochromic and electrochromic technologies, Solar Energy Materials and Solar Cells. 200 (2019). https://doi.org/10.1016/J.SOLMAT.2019.02.041.
[24] A. Kraft, Electrochromism: a fascinating branch of electrochemistry, ChemTexts. 5 (2019). https://doi.org/10.1007/S40828-018-0076-X.
[25] Display Market Size & Share | Industry Report, 2021-2026 | MarketsandMarketsTM, (n.d.). https://www.marketsandmarkets.com/Market-Reports/display-market-925.html (accessed May 24, 2022).
[26] Global Touch Screen Displays Market 2020-2027 - Increasing Penetration of Mobile Devices Presents Enormous Growth Potential - ResearchAndMarkets.com | Business Wire, (n.d.). https://www.businesswire.com/news/home/20200708005693/en/Global-Touch-Screen-Displays-Market-2020-2027---Increasing-Penetration-of-Mobile-Devices-Presents-Enormous-Growth-Potential---ResearchAndMarkets.com (accessed May 24, 2022).
[27] Smart Glass and Smart Window Market Size, Share and Analysis | Forecast - 2030, (n.d.). https://www.alliedmarketresearch.com/smart-glass-and-smart-windows-market (accessed May 24, 2022).
[28] The Outlook for the Global Battery Market, (n.d.). https://internationalbanker.com/brokerage/the-outlook-for-the-global-battery-market/ (accessed May 24, 2022).
[29] Battery Market Size & Share | Industry Report, 2020-2027, (n.d.). https://www.grandviewresearch.com/industry-analysis/battery-market (accessed May 24, 2022).
[30] Supercapacitor Market Size, Share | Future Analysis and Trends by 2027, (n.d.). https://www.alliedmarketresearch.com/supercapacitor-market (accessed May 24, 2022).
[31] R.A. Afre, N. Sharma, M. Sharon, M. Sharon, Transparent conducting oxide films for various applications: A review, Reviews on Advanced Materials Science. 53 (2018) 79–89. https://doi.org/10.1515/RAMS-2018-0006/MACHINEREADABLECITATION/RIS.
[32] C.G. Granqvist, A. Hultåker, Transparent and conducting ITO films: new developments and applications, Thin Solid Films. 411 (2002) 1–5. https://doi.org/10.1016/S0040-6090(02)00163-3.
[33] B.W. Kim, W. Cha, S. Choi, J. Shin, B.S. Choi, M. Kim, Assessment of occupational exposure to indium dust for indium-tin-oxide manufacturing workers, Biomolecules. 11 (2021) 1–14. https://doi.org/10.3390/biom11030419.

[34] H.H. Liu, C.Y. Chen, G.I. Chen, L.H. Lee, H.L. Chen, Relationship between indium exposure and oxidative damage in workers in indium tin oxide production plants, Int Arch Occup Environ Health. 85 (2012) 447–453. https://doi.org/10.1007/S00420-011-0688-6/TABLES/5.

[35] S. Homma, A. Miyamoto, S. Sakamoto, K. Kishi, N. Motoi, K. Yoshimura, Pulmonary fibrosis in an individual occupationally exposed to inhaled indium-tin oxide, European Respiratory Journal. 25 (2005) 200–204. https://doi.org/10.1183/09031936.04.10012704.

[36] T. Homma, T. Ueno, K. Sekizawa, A. Tanaka, M. Hirata, Interstitial pneumonia developed in a worker dealing with dusts containing indium–tin oxide, J Occup Health. 45 (2003) 137–139. https://doi.org/10.1539/joh.45.137.

[37] E.M. Bomhard, The toxicology of indium oxide, Environ Toxicol Pharmacol. 58 (2018) 250–258. https://doi.org/10.1016/j.etap.2018.02.003.

[38] Y. Shi, L. He, Q. Deng, Q. Liu, L. Li, W. Wang, Z. Xin, R. Liu, Synthesis and Applications of Silver Nanowires for Transparent Conductive Films, Micromachines 2019, Vol. 10, Page 330. 10 (2019) 330. https://doi.org/10.3390/MI10050330.

[39] S. Park, M. Vosguerichian, Z. Bao, A review of fabrication and applications of carbon nanotube film-based flexible electronics, Nanoscale. 5 (2013) 1727–1752. https://doi.org/10.1039/C3NR33560G.

[40] D. Tan, C. Jiang, Q. Li, S. Bi, J. Song, Silver nanowire networks with preparations and applications: a review, Journal of Materials Science: Materials in Electronics. 31 (2020) 15669–15696. https://doi.org/10.1007/S10854-020-04131-X/FIGURES/25.

[41] G. Pattan, G. Kaul, Health hazards associated with nanomaterials, Toxicol Ind Health. 30 (2014) 499–519. https://doi.org/10.1177/0748233712459900.

[42] S. Rasras, H. Kalantari, M. Rezaei, M.A. Dehghani, L. Zeidooni, K. Alikarami, F. Dehghani, S. Alboghobeish, Single-walled and multiwalled carbon nanotubes induce oxidative stress in isolated rat brain mitochondria, Toxicol Ind Health. 35 (2019) 497–506. https://doi.org/10.1177/0748233719856983.

[43] A.P. Francis, T. Devasena, Toxicity of carbon nanotubes: A review, Toxicol Ind Health. 34 (2018) 200–210. https://doi.org/10.1177/0748233717747472.

[44] E.K. Sohn, S.A. Johari, T.G. Kim, J.K. Kim, E. Kim, J.H. Lee, Y.S. Chung, I.J. Yu, Aquatic toxicity comparison of silver nanoparticles and silver nanowires, Biomed Res Int. 2015 (2015). https://doi.org/10.1155/2015/893049.

[45] D.E. Gorka, J.S. Osterberg, C.A. Gwin, B.P. Colman, J.N. Meyer, E.S. Bernhardt, C.K. Gunsch, R.T. DiGulio, J. Liu, Reducing Environmental Toxicity of Silver Nanoparticles through Shape Control, Environ Sci Technol. 49 (2015) 10093–10098. https://doi.org/10.1021/ACS.EST.5B01711/SUPPL_FILE/ES5B01711_SI_001.PDF.

[46] H. Shirakawa, E.J. Louis, A.G. MacDiarmid, C.K. Chiang, A.J. Heeger, Synthesis of electrically conducting organic polymers: Halogen derivatives of polyacetylene, (CH)x, J Chem Soc Chem Commun. (1977) 578–580. https://doi.org/10.1039/C39770000578.

[47] C.K. Chiang, C.R. Fincher, Y.W. Park, A.J. Heeger, H. Shirakawa, E.J. Louis, S.C. Gau, A.G. MacDiarmid, Electrical Conductivity in Doped Polyacetylene, Phys Rev Lett. 39 (1977) 1098–1101. https://doi.org/10.1103/PhysRevLett.39.1098.

[48] The Nobel Prize in Chemistry 2000, (n.d.). https://www.nobelprize.org/prizes/chemistry/2000/summary/.

[49] M. Yamaura, T. Hagiwara, K. Iwata, Enhancement of electrical conductivity of polypyrrole film by stretching: Counter ion effect, Synth Met. 26 (1988) 209–224. https://doi.org/10.1016/0379-6779(88)90238-X.

[50] M. v. Fabretto, D.R. Evans, M. Mueller, K. Zuber, P. Hojati-Talemi, R.D. Short, G.G. Wallace, P.J. Murphy, Polymeric material with metal-like conductivity for next generation organic electronic devices, Chemistry of Materials. 24 (2012) 3998–4003. https://doi.org/10.1021/cm302899v.

[51] S.J. Pomfret, P.N. Adams, N.P. Comfort, A.P. Monkman, Inherently Electrically Conductive Fibers Wet Spun from a Sulfonic Acid-Doped Polyaniline Solution**, Advanced

Materials. 10 (1998) 1351–1353. https://onlinelibrary.wiley.com/doi/10.1002/(SICI)1521-4095(199811)10:16%3C1351::AID-ADMA1351%3E3.0.CO;2-8 (accessed June 2, 2022).
[52] J. Metsik, K. Saal, U. Mäeorg, R. Lõhmus, S. Leinberg, H. Mändar, M. Kodu, M. Timusk, Growth of poly(3,4-ethylenedioxythiophene) films prepared by base-inhibited vapor phase polymerization, J Polym Sci B Polym Phys. 52 (2014) 561–571. https://doi.org/10.1002/polb.23450.
[53] Y. Li, X. Hu, S. Zhou, L. Yang, J. Yan, C. Sun, P. Chen, A facile process to produce highly conductive poly(3,4- ethylenedioxythiophene) films for ITO-free flexible OLED devices, J Mater Chem C Mater. 2 (2014) 916–924. https://doi.org/10.1039/c3tc32096k.
[54] B. Winther-Jensen, K. West, Vapor-phase polymerization of 3,4-ethylenedioxythiophene: A route to highly conducting polymer surface layers, Macromolecules. 37 (2004) 4538–4543. https://doi.org/10.1021/ma049864l.
[55] R. Brooke, J.F. Franco-Gonzalez, K. Wijeratne, E. Pavlopoulou, D. Galliani, X. Liu, R. Valiollahi, I. v. Zozoulenko, X. Crispin, Vapor phase synthesized poly(3,4-ethylenedioxythiophene)-trifluoromethanesulfonate as a transparent conductor material, J Mater Chem A Mater. 6 (2018) 21304–21312. https://doi.org/10.1039/C8TA04744H.
[56] R. Yewale, P. Damlin, M. Salomäki, C. Kvarnström, Layer-by-layer approach to engineer and control conductivity of atmospheric pressure vapor phase polymerized PEDOT thin films, Mater Today Commun. 25 (2020). https://doi.org/10.1016/j.mtcomm.2020.101398.
[57] S. Lehtimäki, M. Suominen, P. Damlin, S. Tuukkanen, C. Kvarnström, D. Lupo, Preparation of Supercapacitors on Flexible Substrates with Electrodeposited PEDOT/Graphene Composites, ACS Appl Mater Interfaces. 7 (2015) 22137–22147. https://doi.org/10.1021/acsami.5b05937.
[58] D. DeLongchamp, P.T. Hammond, Layer-by-layer assembly of PEDOT/polyaniline electrochromic devices, Advanced Materials. 13 (2001) 1455–1459. https://doi.org/10.1002/1521-4095(200110)13:19<1455::AID-ADMA1455>3.0.CO;2-7.
[59] J. Liu, M. Agarwal, K. Varahramyan, Glucose sensor based on organic thin film transistor using glucose oxidase and conducting polymer, Sens Actuators B Chem. 135 (2008) 195–199. https://doi.org/10.1016/j.snb.2008.08.009.
[60] J. Lu, N.J. Pinto, A.G. MacDiarmid, Apparent dependence of conductivity of a conducting polymer on an electric field in a field effect transistor configuration, J Appl Phys. 92 (2002) 6033–6038. https://doi.org/10.1063/1.1511291.
[61] T. le Truong, D.O. Kim, Y. Lee, T.W. Lee, J.J. Park, L. Pu, J. do Nam, Surface smoothness and conductivity control of vapor-phase polymerized poly(3,4-ethylenedioxythiophene) thin coating for flexible optoelectronic applications, Thin Solid Films. 516 (2008) 6020–6027. https://doi.org/10.1016/j.tsf.2007.10.114.
[62] P.A. Levermore, L. Chen, X. Wang, R. Das, D.D.C. Bradley, Highly conductive poly(3,4-ethylenedioxythiophene) films by vapor phase polymerization for application in efficient organic light-emitting diodes, Advanced Materials. 19 (2007) 2379–2385. https://doi.org/10.1002/adma.200700614.
[63] J.Y. Kim, M.H. Kwon, Y.K. Min, S. Kwon, D.W. Ihm, Self-assembly and crystalline growth of poly(3,4-ethylenedioxythiophene) nanofilms, Advanced Materials. 19 (2007) 3501–3506. https://doi.org/10.1002/adma.200602163.
[64] J. Bobacka, Potential stability of all-solid-state ion-selective electrodes using conducting polymers as ion-to-electron transducers, Anal Chem. 71 (1999) 4932–4937. https://doi.org/10.1021/ac990497z.
[65] A.A. Argun, A. Cirpan, J.R. Reynolds, The First Truly All-Polymer Electrochromic Devices, Advanced Materials. 15 (2003) 1338–1341. https://doi.org/10.1002/adma.200305038.
[66] S. Kirchmeyer, K. Reuter, Scientific importance, properties and growing applications of poly(3,4-ethylenedioxythiophene), J Mater Chem. 15 (2005) 2077–2088. https://doi.org/10.1039/b417803n.
[67] B.W. Park, L. Yang, E.M.J. Johansson, N. Vlachopoulos, A. Chams, C. Perruchot, M. Jouini, G. Boschloo, A. Hagfeldt, Neutral, polaron, and bipolaron states in pedot prepared by photoelectrochemical polymerization and the effect on charge generation mechanism in the solid-state dye-

sensitized solar cell, Journal of Physical Chemistry C. 117 (2013) 22484–22491. https://doi.org/10.1021/jp406493v.

[68] Y. Yang, W. Yuan, S. Li, X. Yang, J. Xu, Y. Jiang, Manganese dioxide nanoparticle enrichment in porous conducting polymer as high performance supercapacitor electrode materials, Electrochim Acta. 165 (2015) 323–329. https://doi.org/10.1016/j.electacta.2015.03.052.

[69] A. Laforgue, All-textile flexible supercapacitors using electrospun poly(3,4- ethylenedioxythiophene) nanofibers, J Power Sources. 196 (2011) 559–564. https://doi.org/10.1016/j.jpowsour.2010.07.007.

[70] C. Gao, G. Chen, Conducting polymer/carbon particle thermoelectric composites: Emerging green energy materials, Compos Sci Technol. 124 (2016) 52–70. https://doi.org/10.1016/j.compscitech.2016.01.014.

[71] D. Bhattacharyya, R.M. Howden, D.C. Borrelli, K.K. Gleason, Vapor phase oxidative synthesis of conjugated polymers and applications, J Polym Sci B Polym Phys. 50 (2012) 1329–1351. https://doi.org/10.1002/POLB.23138.

[72] L. Bert Groenendaal, F. Jonas, D. Freitag, H. Pielartzik, J.R. Reynolds, Poly(3,4-ethylenedioxythiophene) and Its Derivatives: Past, Present, and Future**, Advanced Materials. 12 (2000) 481–494. https://doi.org/10.1002/(SICI)1521-4095(200004)12:7.

[73] F. Wang, Y.H. Lai, N.M. Kocherginsky, Y.Y. Kosteski, The first fully characterized 1,3-polyazulene: High electrical conductivity resulting from cation radicals and polycations generated upon protonation, Org Lett. 5 (2003) 995–998. https://doi.org/10.1021/ol0274615.

[74] Q. Sun, I.C.Y. Hou, K. Eimre, C.A. Pignedoli, P. Ruffieux, A. Narita, R. Fasel, On-surface synthesis of polyazulene with 2,6-connectivity, Chemical Communications. 55 (2019) 13466–13469. https://doi.org/10.1039/c9cc07168g.

[75] K. Iwasaki, K. Matsumoto, S. Hino, Electrochemical polymerization of alkyl-substituted azulene, Synth Met. 55–57 (1993) 1062–1066.

[76] E. Grądzka, P. Makowska, K. Winkler, Chemically formed conducting polyazulene: From micro- to nanostructures, Synth Met. 246 (2018) 115–121. https://doi.org/10.1016/j.synthmet.2018.10.002.

[77] E. Grodzka, K. Winkler, B.M. Esteban, C. Kvarnstrom, Capacitance properties of electrochemically deposited polyazulene films, Electrochim Acta. 55 (2010) 970–978. https://doi.org/10.1016/j.electacta.2009.09.054.

[78] T. Hirabayashi, K. Naoi, T. Osaka, Application of Electrochemically Formed Polyazulene to Secondary Battery, J Electrochem Soc. 134 (1987) 758–759. https://doi.org/10.1149/1.2100550.

[79] T. Osaka, K. Naoi, T. Hirabayashi, Application of Electrochemically Formed Polyazulene to Rechargeable Lithium Battery, Journal of Electrochemical Society. 134 (1987) 2645–2649.

[80] M. Suominen, S. Lehtimäki, R. Yewale, P. Damlin, S. Tuukkanen, C. Kvarnström, Electropolymerized polyazulene as active material in flexible supercapacitors, J Power Sources. 356 (2017) 181–190. https://doi.org/10.1016/j.jpowsour.2017.04.082.

[81] N. He, L. Höfler, R.M. Latonen, T. Lindfors, Influence of hydrophobization of the polyazulene ion-to-electron transducer on the potential stability of calcium-selective solid-contact electrodes, Sens Actuators B Chem. 207 (2015) 918–925. https://doi.org/10.1016/j.snb.2014.10.048.

[82] M. Suominen, P. Damlin, C. Kvarnström, Probing the interactions in composite of graphene oxide and polyazulene in ionic liquid by in situ spectroelectrochemistry, Electrochim Acta. 284 (2018) 168–176. https://doi.org/10.1016/j.electacta.2018.07.069.

[83] Regulatory AffairsThermo Fisher Scientific, SAFETY DATA SHEET, (n.d.). https://www.fishersci.ca/store/msds?partNumber=AC454930250&productDescription=3-4-ethylenedioxythiophene-99-acros-organics-2&language=en&countryCode=CA (accessed June 2, 2022).

[84] Regulatory AffairsThermo Fisher Scientific, SAFETY DATA SHEET, (n.d.). https://www.fishersci.com/store/msds?partNumber=AC105181000&productDescription=AZULENE%2C+99%25+100MG&vendorId=VN00032119&countryCode=US&language=en (accessed June 2, 2022).

[85] T. Nezakati, B.G. Cousins, A.M. Seifalian, Toxicology of chemically modified graphene-based materials for medical application, Arch Toxicol. 88 (2014) 1987–2012. https://doi.org/10.1007/s00204-014-1361-0.
[86] E. Elkhawass, M. Mohallal, M. Soliman, ACUTE TOXICITY OF DIFFERENT SIZES OF SILVER NANOPARTICLES INTRAPERITONALLY INJECTED IN BALB/C MICE USING TWO TOXICOLOGICAL METHODS, International Journal of Pharmacy and Pharamaceutical Sciences. 7 (2015) 94–99. https://innovareacademics.in/journals/index.php/ijpps/article/view/3776/pdf_579 (accessed June 11, 2022).
[87] Regulatory AffairsThermo Fisher Scientific, SAFETY DATA SHEET: INDIUM(III) OXIDE, (2010). www.alfa.com (accessed June 11, 2022).
[88] S. Mahsan Hoseini-Alfatemi, F. Fallah, S. Armin, M. Hafizi, A. Karimi, S. Kalanaky, Evaluation of Blood and Liver Cytotoxicity and Apoptosis-necrosis Induced by Nanochelating Based Silver Nanoparticles in Mouse Model, Iranian Journal of Pharmaceutical Research. 19 (2020) 207–218. https://doi.org/10.22037/IJPR.2020.1101026.
[89] National Toxicology Program, Chemical Information Profile for Indium Tin Oxide [CAS No. 50926-11-9] Supporting Nomination for Toxicological Evaluation by the National Toxicology Program, 2009. http://ntp.niehs.nih.gov/ (accessed June 9, 2022).
[90] P. Bakun, B. Czarczynska-Goslinska, T. Goslinski, S. Lijewski, In vitro and in vivo biological activities of azulene derivatives with potential applications in medicine, Medicinal Chemistry Research. 30 (2021) 834–846. https://doi.org/10.1007/S00044-021-02701-0.
[91] F.A. Andersen, Final Report on the Safety Assessment of Azulene, Int J Toxicol. 18 (1999) 27–32. https://doi.org/10.1177/109158189901800304.
[92] C. Boehler, Z. Aqrawe, M. Asplund, Applications of PEDOT in bioelectronic medicine, Bioelectron Med (Lond). 2 (2019) 89–99. https://doi.org/10.2217/bem-2019-0014.
[93] C. Pitsalidis, A.-M. Pappa, A.J. Boys, Y. Fu, C.-M. Moysidou, D. van Niekerk, J. Saez, A. Savva, D. Iandolo, R.M. Owens, Organic Bioelectronics for In Vitro Systems, Chem Rev. 122 (2022) 4700–4790. https://doi.org/10.1021/acs.chemrev.1c00539.
[94] S. Rudd, D. Evans, Recent advances in the aqueous applications of PEDOT, Nanoscale Adv. 4 (2022) 733–741. https://doi.org/10.1039/D1NA00748C.
[95] A. Österholm, P. Damlin, C. Kvarnström, A. Ivaska, Studying electronic transport in polyazulene-ionic liquid systems using infrared vibrational spectroscopy, Physical Chemistry Chemical Physics. 13 (2011) 11254–11263. https://doi.org/10.1039/c1cp20246d.
[96] G. Neoh, K, T. Kang, E, C. Tan,T, Chemical synthesis and characterization of electroactive and partially soluble polyazulene, Polymer Bulletin. 19 (1988) 325–331.
[97] S.H. Baxamusa, S.G. Im, K.K. Gleason, Initiated and oxidative chemical vapor deposition: a scalable method for conformal and functional polymer films on real substrates, Physical Chemistry Chemical Physics. 11 (2009) 5227. https://doi.org/10.1039/b900455f.
[98] H. Chelawat, S. Vaddiraju, K. Gleason, Conformal, conducting poly(3,4-ethylenedioxythiophene) thin films deposited using bromine as the oxidant in a completely dry oxidative chemical vapor deposition process, Chemistry of Materials. 22 (2010) 2864–2868. https://doi.org/10.1021/CM100092C/ASSET/IMAGES/LARGE/CM-2010-00092C_0006.JPEG.
[99] S. Lee, D.C. Paine, K.K. Gleason, Heavily doped poly(3,4-ethylenedioxythiophene) thin films with high carrier mobility deposited using oxidative CVD: Conductivity stability and carrier transport, Adv Funct Mater. 24 (2014) 7187–7196. https://doi.org/10.1002/ADFM.201401282.
[100] J.P. Lock, J.L. Lutkenhaus, N.S. Zacharia, S.G. Im, P.T. Hammond, K.K. Gleason, Electrochemical investigation of PEDOT films deposited via CVD for electrochromic applications, Synth Met. 157 (2007) 894–898. https://doi.org/10.1016/J.SYNTHMET.2007.08.022.
[101] S.G. Im, B.S. Kim, L.H. Lee, W.E. Tenhaeff, P.T. Hammond, K.K. Gleason, A Directly Patternable, Click-Active Polymer Film via Initiated Chemical Vapor Deposition, Macromol Rapid Commun. 29 (2008) 1648–1654. https://doi.org/10.1002/MARC.200800404.

[102] S.P. Arnold, J.K. Harris, B. Neelamraju, M. Rudolph, E.L. Ratcliff, Microstructure-dependent electrochemical properties of chemical-vapor deposited poly(3,4-ethylenedioxythiophene) (PEDOT) films, Synth Met. 253 (2019) 26–33. https://doi.org/10.1016/J.SYNTHMET.2019.04.022.
[103] B. Vaagensmith, K.M. Reza, M.N. Hasan, H. Elbohy, N. Adhikari, A. Dubey, N. Kantack, E. Gaml, Q. Qiao, Environmentally Friendly Plasma-Treated PEDOT:PSS as Electrodes for ITO-Free Perovskite Solar Cells, ACS Appl Mater Interfaces. 9 (2017) 35861–35870. https://doi.org/10.1021/acsami.7b10987.
[104] B.J. Worfolk, S.C. Andrews, S. Park, J. Reinspach, N. Liu, M.F. Toney, S.C.B. Mannsfeld, Z. Bao, Ultrahigh electrical conductivity in solution-sheared polymeric transparent films, Proc Natl Acad Sci U S A. 112 (2015) 14138–14143. https://doi.org/10.1073/PNAS.1509958112.
[105] X. Fan, W. Nie, H. Tsai, N. Wang, H. Huang, Y. Cheng, R. Wen, L. Ma, F. Yan, Y. Xia, PEDOT:PSS for Flexible and Stretchable Electronics: Modifications, Strategies, and Applications, Advanced Science. 6 (2019). https://doi.org/10.1002/ADVS.201900813.
[106] A. Sharma, G. Andersson, J. Rivnay, J.F. Alvino, G.F. Metha, M.R. Andersson, K. Zuber, M. Fabretto, Insights into the Oxidant/Polymer Interfacial Growth of Vapor Phase Polymerized PEDOT Thin Films, Adv Mater Interfaces. 5 (2018) 1–8. https://doi.org/10.1002/admi.201800594.
[107] D. Evans, M. Fabretto, M. Mueller, K. Zuber, R. Short, P. Murphy, Structure-directed growth of high conductivity PEDOT from liquid-like oxidant layers during vacuum vapor phase polymerization, J Mater Chem. 22 (2012) 14889–14895. https://doi.org/10.1039/C2JM32281A.
[108] M. Fabretto, C. Jariego-Moncunill, J.P. Autere, A. Michelmore, R.D. Short, P. Murphy, High conductivity PEDOT resulting from glycol/oxidant complex and glycol/polymer intercalation during vacuum vapour phase polymerisation, Polymer (Guildf). 52 (2011) 1725–1730. https://doi.org/10.1016/j.polymer.2011.02.028.
[109] M. Fabretto, K. Zuber, C. Hall, P. Murphy, High Conductivity PEDOT Using Humidity Facilitated Vacuum Vapour Phase Polymerisation, Macromol Rapid Commun. 29 (2008) 1403–1409. https://doi.org/10.1002/marc.200800270.
[110] S.G. Im, K.K. Gleason, Systematic control of the electrical conductivity of poly(3,4- ethylenedioxythiophene) via oxidative chemical vapor deposition, Macromolecules. 40 (2007) 6552–6556. https://doi.org/10.1021/MA0628477/ASSET/IMAGES/LARGE/MA0628477F00007.JPEG.
[111] M.C. Barr, J.A. Rowehl, R.R. Lunt, J. Xu, A. Wang, C.M. Boyce, S.G. Im, V. Bulović, K.K. Gleason, Direct Monolithic Integration of Organic Photovoltaic Circuits on Unmodified Paper, Advanced Materials. 23 (2011) 3500–3505. https://doi.org/10.1002/ADMA.201101263.
[112] D.O. Kim, P.C. Lee, S.J. Kang, K. Jang, J.H. Lee, M.H. Cho, J. do Nam, In-situ blends of polypyrrole/poly(3,4-ethylenedioxythiopene) using vapor phase polymerization technique, Thin Solid Films. 517 (2009) 4156–4160. https://doi.org/10.1016/J.TSF.2009.02.028.
[113] A. Laforgue, L. Robitaille, Deposition of ultrathin coatings of polypyrrole and poly(3,4- ethylenedioxythiophene) onto electrospun nanofibers using a vapor-phase polymerization method, Chemistry of Materials. 22 (2010) 2474–2480. https://doi.org/10.1021/CM902986G/ASSET/IMAGES/LARGE/CM-2009-02986G_0007.JPEG.
[114] T. le Truong, N.D. Luong, J. do Nam, Y. Lee, H.R. Choi, J.C. Koo, H.N. Nguyen, Poly(3,4-ethylenedioxythiophene) vapor-phase polymerization on glass substrate for enhanced surface smoothness and electrical conductivity, Macromol Res. 15 (2007) 465–468. https://doi.org/10.1007/bf03218815.
[115] Y.H. Han, J. Travas-Sejdic, B. Wright, J.H. Yim, Simultaneous Vapor-Phase Polymerization of PEDOT and a Siloxane into Organic/Inorganic Hybrid Thin Films, Macromol Chem Phys. 212 (2011) 521–530. https://doi.org/10.1002/MACP.201000634.
[116] S. Admassie, F. Zhang, A.G. Manoj, M. Svensson, M.R. Andersson, O. Inganäs, A polymer photodiode using vapour-phase polymerized PEDOT as an anode, Solar Energy Materials and Solar Cells. 90 (2006) 133–141. https://doi.org/10.1016/J.SOLMAT.2005.02.005.
[117] N. Vucaj, M.D.J. Quinn, C. Baechler, S.M. Notley, P. Cottis, P. Hojati-Talemi, M. v. Fabretto, G.G. Wallace, P.J. Murphy, D.R. Evans, Vapor phase synthesis of conducting polymer

nanocomposites incorporating 2D nanoparticles, Chemistry of Materials. 26 (2014) 4207–4213. https://doi.org/10.1021/CM5014653/SUPPL_FILE/CM5014653_SI_001.PDF.

[118] M.A. Ali, H. Kim, C. Lee, H. Nam, J. Lee, Effects of iron(III) p-toluenesulfonate hexahydrate oxidant on the growth of conductive poly(3,4-ethylenedioxythiophene) (PEDOT) nanofilms by vapor phase polymerization, Synth Met. 161 (2011) 1347–1352. https://doi.org/10.1016/J.SYNTHMET.2011.04.036.

[119] O. Bubnova, Z.U. Khan, A. Malti, S. Braun, M. Fahlman, M. Berggren, X. Crispin, Optimization of the thermoelectric figure of merit in the conducting polymer poly(3,4-ethylenedioxythiophene), Nature Materials 2011 10:6. 10 (2011) 429–433. https://doi.org/10.1038/nmat3012.

[120] M.S. Cho, S.Y. Kim, J.D. Nam, Y. Lee, Preparation of PEDOT/Cu composite film by in situ redox reaction between EDOT and copper(II) chloride, Synth Met. 158 (2008) 865–869. https://doi.org/10.1016/J.SYNTHMET.2008.06.003.

[121] I. Horcas, R. Fernández, J.M. Gómez-Rodríguez, J. Colchero, J. Gómez-Herrero, A.M. Baro, WSXM: A software for scanning probe microscopy and a tool for nanotechnology, Review of Scientific Instruments. 78 (2007). https://doi.org/10.1063/1.2432410.

[122] A.K. Poddar, S.S. Patel, H.D. Patel, Synthesis, characterization and applications of conductive polymers: A brief review, Polym Adv Technol. 32 (2021) 4616–4641. https://doi.org/10.1002/PAT.5483.

[123] S. Srilalitha, K.N. Jayaveera, S.S. Madhvendhra, THE EFFECT OF DOPANT, TEMPERATURE AND BAND GAP ON CONDUCTIVITY OF CONDUCTING POLYMERS, Int J Innov Res Sci Eng Technol. 2 (2013) 2319–8753. www.ijirset.com (accessed June 5, 2022).

[124] Modern Physical Organic Chemistry - Eric V. Anslyn, Dennis A. Dougherty - Google Books, (n.d.). https://books.google.fi/books?id=gY-Sxijk_tMC&printsec=frontcover&redir_esc=y#v=onepage&q&f=false (accessed June 7, 2022).

[125] W. Plieth, Intrinsically Conducting Polymers, Electrochemistry for Materials Science. (2008) 323–363. https://doi.org/10.1016/B978-044452792-9.50013-0.

[126] P. Damlin, Electrochemical Polymerization of Poly(paraphenylene vinylene): An electrochemical and Spectroelectrochemical Study on Synthesis and redox processes, Åbo Akademi University, 2001.

[127] Anna. Österholm, Electronic and structural properties of polyazulene materials : an in situ spectroelectrochemical investigation, Åbo Akademy University, 2011.

[128] P. Damlin, C. Kvarnström, A. Ivaska, Spectroelectrochemical characterization of thin fullerene films in room temperature ionic liquids, Journal of Electroanalytical Chemistry. 590 (2006) 190–197. https://doi.org/10.1016/j.jelechem.2006.03.009.

[129] P. Damlin, C. Kvarnström, A. Ivaska, Electrochemical synthesis and in situ spectroelectrochemical characterization of poly(3,4-ethylenedioxythiophene) (PEDOT) in room temperature ionic liquids, Journal of Electroanalytical Chemistry. 570 (2004) 113–122. https://doi.org/10.1016/j.jelechem.2004.03.023.

[130] The Nobel Prize in Physics 1986, (n.d.). https://www.nobelprize.org/prizes/physics/1986/summary/ (accessed June 8, 2022).

[131] G. Binnig, C.F. Quate, C. Gerber, Atomic force microscope, Phys Rev Lett. 56 (1986) 930–933. https://doi.org/10.1103/PHYSREVLETT.56.930/FIGURE/1/THUMB.

[132] D. Triampo, W. Triampo, The Working of the Atomic Force Microscope for Chemical Mapping, The Open Materials Science Journal. 3 (2009) 50–55. http://nobelprize.org/nobel_prizes/physics/laureates/1986/index.html (accessed June 8, 2022).

[133] Scanning Electron Microscopy | Electrons in SEM | Thermo Fisher Scientific - FI, (n.d.). https://www.thermofisher.com/fi/en/home/materials-science/learning-center/applications/sem-electrons.html (accessed June 8, 2022).

[134] Scanning Electron Microscopy and X-Ray Microanalysis - Joseph I. Goldstein, Dale E. Newbury, Joseph R. Michael, Nicholas W.M. Ritchie, John Henry J. Scott, David C. Joy - Google Books, (n.d.).

https://books.google.fi/books?hl=en&lr=&id=D0I_DwAAQBAJ&oi=fnd&pg=PR5&dq=Scanning+Electron+Microscopy+and+X-Ray+Microanalysis%E2%80%9D,+Kluwer+Academic,+New+York.+(2003)&ots=36PI7pCmno&sig=IjC-etsG1NstXdFytw-RkD81FHo&redir_esc=y#v=onepage&q&f=false (accessed June 8, 2022).

[135] A. Mohammed, A. Abdullah, SCANNING ELECTRON MICROSCOPY (SEM): A REVIEW, in: International Conference on Hydraulics and Pneumatics - Hervex, 2018: pp. 77–85.

[136] M. Suominen, Electrochemical fabrication of nanocomposites towards sustainable energy applications, University of Turku, 2019. https://www.utupub.fi/handle/10024/146731 (accessed June 9, 2022).

[137] Basics of EIS: Electrochemical Research-Impedance Gamry Instruments, (n.d.). https://www.gamry.com/application-notes/EIS/basics-of-electrochemical-impedance-spectroscopy/ (accessed June 9, 2022).

[138] M. Ates, Review study of electrochemical impedance spectroscopy and equivalent electrical circuits of conducting polymers on carbon surfaces, Prog Org Coat. 71 (2011) 1–10. https://doi.org/10.1016/J.PORGCOAT.2010.12.011.

TURUN
YLIOPISTO
UNIVERSITY
OF TURKU

Painosalama Oy, Turku, Finland 2022

ISBN 978-951-29-9091-7 (PRINT)
ISBN 978-951-29-9092-4 (PDF)
ISSN 0082-7002 (Print)
ISSN 2343-3175 (Online)